

TopoPrune: Robust Data Pruning via Unified Latent Space Topology

Arjun Roy¹ Prajna G. Malettira¹ Manish Nagaraj¹ Kaushik Roy¹

Abstract

Geometric data pruning methods, while practical for leveraging pretrained models, are fundamentally unstable. Their reliance on extrinsic geometry renders them highly sensitive to latent space perturbations, causing performance to degrade during cross-architecture transfer or in the presence of feature noise. We introduce TopoPrune, a framework which resolves this challenge by leveraging topology to capture the stable, intrinsic structure of data. TopoPrune operates at two scales, (1) utilizing a *topology-aware manifold approximation* to establish a global low-dimensional embedding of the dataset. Subsequently, (2) it employs *differentiable persistent homology* to perform a local topological optimization on the manifold embeddings, ranking samples by their structural complexity. We demonstrate that our *unified dual-scale topological approach* ensures high accuracy and precision, particularly at significant dataset pruning rates (e.g., 90%). Furthermore, through the inherent stability properties of topology, TopoPrune is (a) exceptionally robust to noise perturbations of latent feature embeddings and (b) demonstrates superior transferability across diverse network architectures. This study demonstrates a promising avenue towards stable and principled topology-based frameworks for robust data-efficient learning.

1. Introduction

The computational demands of training modern deep learning systems have escalated dramatically due to the scale of contemporary models and datasets. This growth has made training and fine-tuning computationally prohibitive, creating a need for data-efficient learning strategies. Data pruning is one such strategy that aims to subsample a large dataset into a smaller, representative subset (or coresset) that

¹Department of Electrical and Computer Engineering, Purdue University, U.S.A. Correspondence to: Arjun Roy <roy208@purdue.edu>.

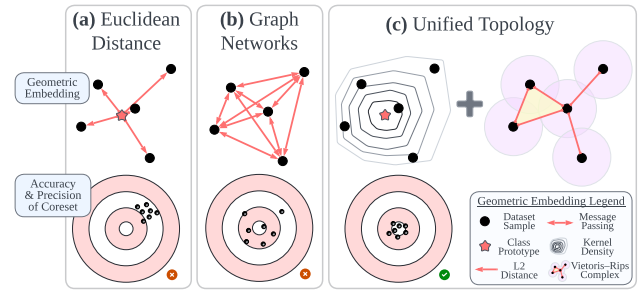


Figure 1. Topological data selection yields higher-performing and stable coressets. Coreset performance across multiple runs reveals the limitations of common methods. (a) Euclidean-based selection is stable but achieves lower accuracy. (b) Graph-based methods achieve higher accuracy but are highly variable. (c) Our topological approach achieves both high accuracy and stability.

preserves the essential learning characteristics of the full dataset. Thereby enabling rapid model training, efficient fine-tuning, and reduced storage costs, all while minimizing degradation in final model performance.

Broadly, coresset selection methods can be categorized into three major categories. *Optimization-based* methods select a coresset whose loss landscape (Killamsetty et al., 2021b; Mindermann et al., 2022) or gradient dynamics (Mirza-soleiman et al., 2019; Killamsetty et al., 2021a; Tan et al., 2023) most closely align with that of the entire dataset, ensuring that a model trained on the subset exhibits comparable generalization. While often effective, such approaches are hampered by significant practical limitations such as their reliance on computationally intensive second-order (Pooladzandi et al., 2022) or bilevel optimization (Borsos et al., 2020). *Score-based* methods rank and choose training samples based on model prediction scores. These can include scores derived from training dynamics (Toneva et al., 2019; Garg & Roy, 2023; Zheng et al., 2025) and uncertainty estimations (Paul et al., 2021; He et al., 2023; 2024; Cho et al., 2025). However, these scores are inherently model and training-dependent and reflect the knowledge of a specific network at a specific point in training. This makes optimization and score-based methods not only expensive, as they require training from scratch for some amount of time, but also incompatible with the vast and growing ecosystem of publicly available pretrained models, where only the final weights are accessible.

To overcome this constraint, *geometry-based* coresets selection methods can operate on static feature embeddings from a pretrained model. Approaches in this domain range from representing samples based on the penultimate-layer feature embedding space (Xia et al., 2023), measuring distributional similarity via optimal transport (Xiao et al., 2024) or Wasserstein distance (Xiong et al., 2024), or using the geometric reconstruction error of samples with decision boundary information (Yang et al., 2024). While these methods avoid costly training analysis, a significant limitation is their reliance on metrics that are sensitive to the extrinsic geometry of the feature embedding space, a vulnerability we term "geometric brittleness" (Papillon et al., 2025). This brittleness leads to two primary shortcomings: (1) a tendency to prioritize samples from dense regions at the expense of informative samples from the sparse tails of the distribution (Zheng et al., 2023), and (2) an instability in performance across different network architectures or when noise is introduced to the embeddings. This is most apparent in Euclidean-distance metrics (Xia et al., 2023) or message-passing graph methods (Maharana et al., 2024; Xie et al., 2025), which are highly sensitive to changes in the feature embedding space (see Fig. 1).

In this work, we introduce TopoPrune, a novel framework that resolves the challenge of geometric brittleness by leveraging topological analysis (Seifert & Threlfall, 1980). To those unfamiliar, topology is a branch of geometry concerned with the properties of a space that are preserved under continuous deformations like stretching and bending, but not tearing. A classic example is that, in a topological sense, a coffee mug and a donut are equivalent as one can be deformed into the other while preserving the single hole that defines them both. By focusing on this stable, intrinsic structure (the hole) rather than the transient, extrinsic geometric measurements (like distance or curvature), we can analyze the feature embeddings of datasets with a stable, topological metric. This allows TopoPrune to achieve exceptional stability to slight perturbations in the feature embedding space, caused by noisy features or those arising from different feature embeddings across architectures (Cohen-Steiner et al., 2005; Suresh et al., 2024). This enables the use of proxy models (Coleman et al., 2020) or the direct use of the vast corpus of pretrained and foundational models to generate coresets without the need for retraining a specific model from scratch.

Our framework first establishes a **global structure** by using *topology-aware manifold approximation* (McInnes et al., 2018a; Wang et al., 2021) to project high-dimensional features into standardized low-dimensional manifold embeddings. While this global structure can group similar samples, it fails to distinguish which samples to prioritize within a localized region. Existing methods often resort to random sampling within localized regions (Zheng et al., 2023) or use

geometric heuristics like message-passing (Maharana et al., 2024). To better complement this global view with **local structure**, we then employ *differentiable persistent homology* (Scoccola et al., 2024; Carrière et al., 2024; Mukherjee et al., 2024) to assess a sample's structural relevancy, relative to its immediate neighbors. Persistent homology tracks the "birth" and "death" (persistence) of topological structures at multiple scales (filtration of a homology group). For our application, we perform an optimization that *maximizes the persistence (the birth and death time) of local topological features* constructed from the filtration of the manifold projected Vietoris–Rips complex (Loiseaux et al., 2023a). This process iteratively repositions samples to an optimal configuration that resolves topological ambiguities and enhances topological stability, directly measuring a sample's contribution to the structural complexity of its local neighborhood. Finally, a unified score consisting of both the global density (of the manifold embeddings) and the local persistence are combined to provide a balance between global and local topological structures.

Our approach makes the following contributions:

- We introduce TopoPrune, a novel coresset selection framework that defines sample importance through a dual-scale topological analysis. It combines a *global manifold projection* with a *local persistence* score derived from a differentiable persistent homology optimization to identify structurally critical samples with higher accuracy and stability compared to previous coresset methods.
- We demonstrate that TopoPrune establishes robust cross-architecture transferability, consistently yielding high-quality coresets regardless of the transfer direction, whether utilizing diverse proxy embeddings (e.g., from ResNet to ViT) for a fixed target model or a single proxy to train a diverse set of target models. This stability enables the use of small proxy models or off-the-shelf pretrained models to generate truly model-agnostic coresets without costly retraining.
- We provide extensive empirical validation showing that TopoPrune significantly outperforms state-of-the-art geometric, gradient, and score-based methods. Our framework delivers coresets with higher accuracy and precision, and is substantially more robust to noisy feature embeddings, especially at high data pruning rates.

By defining sample importance through the stable, intrinsic properties of topology, TopoPrune moves beyond brittle geometric metrics to deliver a truly robust coresset framework.

2. Background and Related Work

2.1. Topology at Two Scales

While many modern topological algorithms inherently model both the global and local structure of data simultaneously, our work decouples these concepts into two distinct stages. For the purposes of this paper, we define global topology as the manifold structure of the entire dataset, which we capture as a low-dimensional embedding. We then define local topology as the fine-grained structure arising from the interactions between samples and their immediate neighbors, which we analyze using persistent homology.

Low-Dimensional Manifold Approximations. A critical step in high-dimensional analysis is creating a low-dimensional data representation. Linear methods like Principal Component Analysis (PCA) (Pearson, 1901) are efficient but preserve only global variance, failing to capture complex non-linear structures. In contrast, non-linear techniques like t-Distributed Stochastic Neighbor Embedding (t-SNE) (van der Maaten & Hinton, 2008) excel at preserving fine-grained local neighborhoods, but this focus often distorts the data’s overall global structure. More recent techniques directly leverage principles from topology to create more faithful manifold embeddings. State-of-the-art methods like Uniform Manifold Approximation and Projection (UMAP) (McInnes et al., 2018a) and PaCMAP (Wang et al., 2021) model high-dimensional data as a fuzzy topological structure to preserve both fine-grained local connectivity and large-scale global relationships.

While learning-based alternatives such as Topological Autoencoders (TopoAE) (Moor et al., 2020) and Regularized TDA (RTD) (Trofimov et al., 2023) offer powerful global topology preservation, they require computationally expensive training and often yield less distinct class separation on complex datasets (see Section B.1.2 for details). Therefore, we prioritize algorithmic solutions like UMAP for their superior efficiency and alignment with our lightweight, training-free objective. These algorithmic methods have proven highly effective for interpreting the complex representations learned by deep models across numerous domains, from single-cell genomics (Becht et al., 2018) to clustering in dictionary learning (Fel et al., 2023; 2024). As shown by (de Bodt et al., 2025), these techniques produce embeddings with compact and well-defined clusters, enhancing the impact of downstream analysis. While the quantitative fidelity of such embeddings is an area of active research (Jeon et al., 2025), we believe that they are well-suited for our task. By explicitly preserving the nearest-neighbor structure from the high-dimensional space, methods such as UMAP and PacMAP inherently maintain the density landscape of the data manifold. This directly preserves the notions of “prototypicality” (samples in high-density regions) and “atypical-

ity” (samples in sparse regions), making the embedding a reliable foundation for our subsequent sample importance scoring (see Section A.3 for a qualitative explanation).

Interactions of Samples and their Nearest Neighbors.

Understanding the local interactions between a sample and its neighbors is crucial for determining its importance. A prevalent approach is the use of Graph Neural Networks (GNNs), which propagate information between nodes on a graph typically defined by nearest-neighbor relationships. In GNNs, a sample’s importance is quantified through learned message-passing that aggregates features from its local neighborhood (Maharana et al., 2024). Other methods use graph-level structural entropy combined with Shapley values and blue noise sampling (Chen et al., 2014) to select a diverse coresset (Xie et al., 2025). However, these approaches operate on a single, fixed graph and can be sensitive to the geometric hyperparameters used in its construction.

In contrast, persistent homology (Botnan & Lesnick, 2022) offers a fundamentally different and more robust framework. Instead of analyzing a single graph, it studies the evolution of higher-order topological structures (e.g., connected components, loops, voids) across a multi-scale filtration of simplicial complexes. This provides a complete summary of the data’s shape at all scales simultaneously. A key advantage of persistent homology is its proven stability (Cohen-Steiner et al., 2005). The persistence diagram of a dataset is guaranteed to change only slightly in response to small perturbations of the input data, making it a robust descriptor of local structure (Turkes et al., 2022; Mishra & Motta, 2023). Inclusion of these robust geometric descriptors has been widely used for understanding feature embeddings in machine learning applications such as monitoring generalization in networks over training (Birdal et al., 2021) and exploring the topology of latent embeddings throughout network layers (Naitzat et al., 2020). For a detailed overview on the underlying construction of simplicial complexes and persistent homology, please see Section A.1.

While traditional persistent homology provides a powerful descriptive tool, its integration into modern deep learning pipelines has been limited as it is not inherently differentiable. Recent advances in differentiable persistent homology have overcome this barrier by enabling the backpropagation of gradients from the persistence diagram back to the coordinates of the input data points (Carrière et al., 2024; Mukherjee et al., 2024). This allows for the direct optimization of the data’s topological features within a gradient-based framework. The work of (Scoccolla et al., 2024) provides a fast and stable computational framework for these gradients, even for the more expressive case of multiparameter persistent homology. By leveraging this, rather than simply describing static local topology, we can perform an optimization to actively enhance it.

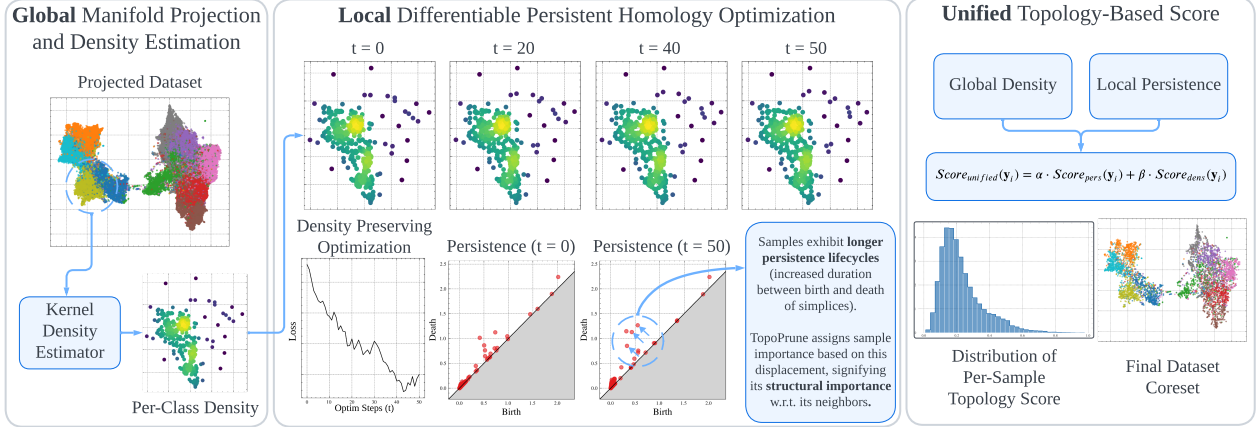


Figure 2. An overview of TopoPrune. (Left) A topology-aware projection visualizes the *global* data manifold. (Middle) Within each class, a density-preserving persistent homology optimization derives a *local* persistence score per sample. The color map indicates high (yellow) to low (blue) density. (Right) The final coresset is constructed via stratified sampling on a unified score combining *global density* and *local persistence*. This not only prioritizes the most topologically informative samples but also faithfully represents the density distribution of the original dataset.

3. Methodology

Our proposed method, TopoPrune, constructs a coresset by analyzing the data’s topological structure at two distinct scales. (1) *Global Manifold Embedding*, projects the original high-dimensional embeddings into a standardized low-dimensional space. This ensures a stable, global view of the data’s overall structure. (2) *Local Topological Interaction*, which employs differentiable multi-parameter persistent homology to probe the local structure formed by samples and their closest neighbors. Together, these two topological scales are used to derive an importance score for each sample based on global density and local persistent homology, contributing to a unified topological measurement for selecting individual samples (see Fig. 2).

3.1. Global Structure: Dataset Representation with Topological Manifold Embedding

Given a well-trained deep model, denoted by $f(\cdot)$, we can express it as a composition of a feature extractor $h(\cdot)$ and a classifier $g(\cdot)$, such that $f(\cdot) = g(h(\cdot))$. Here, $h(\cdot)$ represents the network up to the *penultimate layer*, which maps an input data point \mathbf{x} to a high-dimensional feature embedding $\mathbf{z} = h(\mathbf{x}) \in \mathbb{R}^D$. The full dataset $\mathcal{D} = \{(\mathbf{x}_1, y_1), \dots, (\mathbf{x}_N, y_N)\}$ can thus be transformed into a high-dimensional feature set $Z = \{\mathbf{z}_1, \dots, \mathbf{z}_N\}$. While this high-dimensional space Z contains rich semantic information, its extrinsic geometry is often complex and architecture-dependent. To obtain a stable and standardized representation, we project Z onto a low-dimensional manifold using topology-based manifold approximation and projection techniques (McInnes et al., 2018a; Wang et al., 2021).

This process involves two main stages. First, a topological representation of the high-dimensional data is constructed as a fuzzy simplicial set. This structure captures the data’s shape by assigning a membership strength (p_{ij}), to the potential connections between each point and its neighbors, where the “fuzzy” aspect represents the belief that a certain simplex exists in the true underlying manifold. Subsequently, a low-dimensional embedding is learned $Y = \{\mathbf{y}_1, \dots, \mathbf{y}_N\}$, where $\mathbf{y}_i \in \mathbb{R}^d$ and $d \ll D$, whose own fuzzy simplicial set (q_{ij}) is similarly defined. The final low-dimensional representation Y is found by optimizing the positions of the points $\{\mathbf{y}_i\}$ to minimize a cross-entropy loss between the high-dimensional (p_{ij}) and low-dimensional (q_{ij}) pairwise similarities:

$$\mathcal{L}_{\text{proj}}(Y) = \sum_{i \neq j} \left[p_{ij} \log \left(\frac{p_{ij}}{q_{ij}} \right) + (1 - p_{ij}) \log \left(\frac{1 - p_{ij}}{1 - q_{ij}} \right) \right] \quad (1)$$

This process yields a standardized manifold embedding that preserves the data’s intrinsic shape. Through a detailed investigation into different manifold approximation and projection techniques presented in Section B.1 we use UMAP (McInnes et al., 2018a) as it creates more uniform manifold embeddings across network architectures (see Section C.4 exploring UMAP hyperparameters). On this low-dimensional manifold, we compute a **Density Score** for each sample using a Kernel Density Estimator (KDE), to capture its global representativeness. This estimates the probability density at each sample \mathbf{y}_i by summing the contributions of neighboring points $\sum_{j=1}^n \mathbf{y}_j$:

$$\text{Score}_{\text{dens}}(\mathbf{y}_i) = \frac{1}{Nh} \sum_{j=1}^N K \left(\frac{\mathbf{y}_i - \mathbf{y}_j}{h} \right) \quad (2)$$

where N is the number of samples, K is a Gaussian kernel, and h is the bandwidth parameter. This score allows us to distinguish samples in high-density (prototypical) regions from those in low-density (atypical) regions of the manifold.

3.2. Local Structure: Sample Neighborhoods with Persistence-Based Optimizer

The global manifold embedding provides a low-dimensional representation that faithfully preserves the global structure of the data manifold. While this ensures a stable, high-level representation, a purely global perspective is insufficient for identifying the most informative samples, which is often defined by the complex local interactions with their nearest neighbors. To capture this fine-grained structure, we leverage persistent homology not as a static descriptor, but as a dynamic topological optimization process. The objective of this process is to iteratively adjust the position of each point within its class manifold to maximize persistence life-cycles (increasing the duration between birth and death of simplicial complex's). This is performed independently for each class $c \in \{1, \dots, C\}$ to analyze the specific intra-class structure. For each class, we begin with its point cloud from the global manifold embedding $Y_c = \{\mathbf{y}_i \mid \text{label}(\mathbf{y}_i) = c\}$ and construct a Vietoris-Rips filtration (Oudot, 2015) on Y_c due to its computational scalability compared to Alpha and Čech complexes (Otter et al., 2017; Mishra & Motta, 2023).

Similar to work from (Scoccola et al., 2024) we define a differentiable loss function, $\mathcal{L}_{\text{pers}}(Y_c)$, whose negative gradient, $-\nabla_{Y_c} \mathcal{L}_{\text{pers}}$, points in the direction that *maximally increases the persistence life-cycle of samples*. This loss is formulated using a multi-parameter filtration considering two parameters: (1) the class-manifold Vietoris-Rips filtration (VR_{Y_c}) and (2) the class-manifold Kernel Density Estimator ($\hat{f} = KDE_{Y_c}$). The persistence of this two-parameter filtration is summarized using the Hilbert decomposition signed measure, of homology degree 1 (H_1), denoted $\mu_{H_1(VR_{Y_c}, \hat{f})}^{Hil}$ (Loiseaux et al., 2023b). This descriptor represents the persistence diagram as a finite collection of positive point masses (representing feature births) and negative point masses (representing feature deaths) in the parameter space of (distance, density). Our objective is to maximize persistence life-cycles, which is accomplished by maximizing the Optimal Transport (OT) distance between this signed measure and the zero measure, $\mathbf{0}$ (Carriere et al., 2021). The differentiable loss function for a given class c is therefore defined as:

$$\mathcal{L}_{\text{pers}}(Y_c) = \text{OT}(\mu_{H_1(VR_{Y_c}, \hat{f})}^{Hil}, \mathbf{0}) \quad (3)$$

The optimization seeks a new point configuration Y'_c that minimizes this loss, solved iteratively via gradient descent (see Section C.1 exploring the number of optimization steps). This specific formulation ensures that the optimization *en-*

hances topological stability while preserving the original density of the class manifold, as the density is recomputed at each epoch and is an integral part of the loss calculation. We then define the **Persistence Score** for each sample \mathbf{y}_i belonging to class c as the magnitude of its total displacement during its class-specific optimization, where \mathbf{y}_i is the initial position and \mathbf{y}'_i is the final, optimized position.:

$$\text{Score}_{\text{pers}}(\mathbf{y}_i) = \|\mathbf{y}_i - \mathbf{y}'_i\|_2, \quad \text{for } \mathbf{y}_i \in Y_c, \mathbf{y}'_i \in Y'_c \quad (4)$$

Interpreting this notion of local dataset structure. A high Persistence Score quantifies the degree of topological instability a sample introduces within its own class manifold. Crucially, our optimization process is designed to be density-preserving, it enhances local topological features without altering the overall density distribution of the class manifold. This is vital for coresnet selection, as it ensures our search for structurally important samples does not distort the global representativeness of the data. The optimization process repositions these points to clarify the underlying intra-class structure and increase its persistence life-cycle. Therefore, the *magnitude of this corrective displacement serves as a direct, dynamic measure of a sample's contribution to the topological complexity of its class*, derived from the collective interaction of every point in the manifold.

3.3. Comprehensive Score with Global and Local Dataset Structures

To create a comprehensive sample importance metric, we formulate a final score that unifies the global density and local persistence information as a weighted combination of these two metrics:

$$\text{Score}_{\text{unified}}(\mathbf{y}_i) = \alpha \cdot \text{Score}_{\text{pers}}(\mathbf{y}_i) + \beta \cdot \text{Score}_{\text{dens}}(\mathbf{y}_i) \quad (5)$$

where hyperparameters $\alpha, \beta \in [0, 1]$ modulate the influence of local topological complexity (Persistence Score) versus global distributional rarity (Density Score). From an exploration across different ranges of α and β in Section C.2 we find that $\alpha = 0.5$ and $\beta = 0.5$ provide a good balance between global and local information. This allows our framework to construct a coresnet that is not only rich in challenging, boundary-defining examples but also maintains a faithful representation of the full dataset's underlying distribution.

3.4. A Training-Free Proxy for Mislabeled Samples

Inspired by findings in CCS (Zheng et al., 2023), we ensure our coresnet is not corrupted by noisy or mislabeled data, which can receive high importance scores yet degrade model performance (Swayamdipta et al., 2020). We incorporate a filtering step to create a clean dataset $\mathcal{D}_{\text{clean}} = \mathcal{D} \setminus \mathcal{I}_{\text{mis}}$ where \mathcal{I}_{mis} are the mislabeled sample indices. While most

recent methods, including CCS and D2 (Maharana et al., 2024), use training-dynamic metrics like Area Under the Margin (AUM) (Pleiss et al., 2020) to identify mislabeled samples, this diverges from our ultimate goal to operate solely on static embeddings from pretrained models.

To overcome this, we propose a training-free proxy for AUM, which we term the Neighborhood Label Purity Score (NLPS). For each sample, we compute the fraction of its k -nearest neighbors in the latent space that share its class label. A low NLPS indicates that a sample resides in a mixed-label neighborhood, suggesting it is on a noisy decision boundary or potentially mislabeled, analogous to the "flip-flop" candidates identified by AUM. We validate this approach by exploring multiple AUM proxies, as shown in Section C.3 and follow standard mislabel ratios as established by Zheng et al. (2023) as shown in Appendix Table 13.

3.5. Topological Stratification and Coreset Construction

In the final phase, we construct the coreset from the remaining "clean" dataset (\mathcal{D}_{clean}). We perform stratified sampling based on the calculated Score_{unified} to select samples which strictly preserves the original class distribution for a desired pruning rate, as shown in Zheng et al. (2023). Importantly, TopoPrune generates an *unbalanced* coreset, rather than enforcing a uniform number of samples per class, we respect the intrinsic class imbalance of the original dataset structure. This process yields a coreset that is topologically rich and globally representative.

In summary, TopoPrune includes three distinct phases: (1) Dual-scale topological scoring (projecting global manifolds and optimizing local persistence), (2) Mislabeled sample filtering (creating a "clean" dataset removing mislabeled samples), and (3) Topological selection (stratified sampling on the "clean" dataset based on the unified topology score). For further implementation details, we provide the complete pseudocode in Section B.2 and an illustrative example of the selection process in Section A.4.

4. Results

4.1. Experimental Setup

TopoPrune utilizes several tools and frameworks. Manifold projection is performed using UMAP (McInnes et al., 2018b), multipers (Loiseaux & Schreiber, 2024) facilitates differential persistent homology which uses the Gudhi C++ library (Maria et al., 2025) as a backend, and DeepCore (Guo et al., 2022) is used to standardize coreset selection and training across different methods.

To ensure fair comparisons in our experiments, we evaluate two versions of our framework. When benchmarking against other training-free methods, we use *TopoPrune*

(*NLPS*), which incorporates NLPS for mislabeled samples. When comparing against methods that require training-time information, we use *TopoPrune*, which incorporates the original AUM score. We compare **TopoPrune (NLPS)** with several static geometry-based coresnet selection methods: A) **Random** selection. B) **Moderate** (Xia et al., 2023) uses samples near the median distance to a class prototype (the barycenter of a point-mass distribution). C) **FDMat** (Xiao et al., 2024) matches data distribution between dataset and coresnet using optimal transport. We compare **TopoPrune** with several geometry, score, and optimization-based methods that require training-time information: D) **Moderate (AUM)** incorporating Moderate with AUM-based mislabeled removal. E) **Forgetting** (Toneva et al., 2019) uses the number of times an example is incorrectly classified after being correctly classified earlier during training. F) **Glister** (Killamsetty et al., 2021b) uses bi-level optimization. G) **LCMat-S** (Shin et al., 2023) matches loss curvature between dataset and coresnet. H) **CCS** (Zheng et al., 2023) uses stratified sampling of difficulty scores (such as AUM or Forgetting) with intra-strata random sampling. H) **D2** (Ma-

Table 1. Accuracy across coresnet selection methods on CIFAR-10, CIFAR-100 and ImageNet-1K. TopoPrune's advantages (accuracy and precision) are most pronounced on challenging datasets like ImageNet-1K and at high pruning rates (e.g., 90%).

		Pruning Rate (\rightarrow)	30%	50%	70%	80%	90%
CIFAR-10 (ResNet-18)							
<i>No Training Dynamics</i>	Random	94.5 \pm 0.1	93.5 \pm 0.1	90.8 \pm 0.2	86.6 \pm 0.3	76.7 \pm 0.9	
	Moderate	94.2 \pm 0.1	93.1 \pm 0.1	89.9 \pm 0.2	87.2 \pm 0.2	76.9 \pm 1.0	
	FDMat	94.7 \pm 0.1	93.6 \pm 0.2	90.8\pm0.2	87.3 \pm 0.4	74.4 \pm 0.7	
	TopoPrune (NLPS)	94.8\pm0.1	93.6\pm0.2	90.3 \pm 0.2	87.3\pm0.3	77.1\pm0.6	
<i>With Training Dynamics</i>	Moderate (AUM)	93.9 \pm 0.2	93.1 \pm 0.2	90.1 \pm 0.2	87.1 \pm 0.2	79.9 \pm 0.3	
	Forgetting	94.5 \pm 0.2	92.6 \pm 0.1	89.8 \pm 0.2	85.6 \pm 0.3	67.6 \pm 0.4	
	Glister	94.4 \pm 0.2	93.8 \pm 0.2	90.8 \pm 0.4	85.1 \pm 0.6	66.8 \pm 1.3	
	LCMat-S	94.5 \pm 0.2	93.3 \pm 0.2	90.5 \pm 0.2	86.9 \pm 0.2	75.1 \pm 0.8	
	CCS	95.5 \pm 0.1	94.8 \pm 0.2	93.0 \pm 0.2	90.7\pm0.2	81.9 \pm 0.7	
	D2	95.6\pm0.1	94.8\pm0.1	93.1\pm0.1	89.2 \pm 0.2	80.9 \pm 1.5	
	TopoPrune	94.7 \pm 0.2	93.7 \pm 0.2	91.6 \pm 0.1	88.7 \pm 0.4	82.1\pm0.3	
CIFAR-100 (ResNet-18)							
<i>No Training Dynamics</i>	Random	75.3 \pm 0.2	71.6 \pm 0.1	63.7 \pm 0.5	55.9 \pm 1.0	34.0 \pm 1.1	
	Moderate	74.9 \pm 0.3	70.1 \pm 0.3	63.7 \pm 0.2	56.1 \pm 0.5	34.9 \pm 2.1	
	FDMat	75.4 \pm 0.2	71.9\pm0.3	64.0 \pm 0.6	56.1 \pm 1.5	37.5 \pm 1.6	
	TopoPrune (NLPS)	75.6\pm0.2	71.9\pm0.2	65.3\pm0.4	56.7\pm0.4	41.6\pm0.8	
<i>With Training Dynamics</i>	Moderate (AUM)	75.9 \pm 0.3	72.4 \pm 0.2	66.7 \pm 0.3	60.2 \pm 0.8	40.0 \pm 1.2	
	Forgetting	74.8 \pm 0.2	67.2 \pm 0.9	50.6 \pm 0.7	32.3 \pm 0.9	24.3 \pm 1.4	
	Glister	75.8 \pm 0.3	70.7 \pm 0.7	66.1 \pm 1.2	54.7 \pm 1.6	38.4 \pm 1.7	
	LCMat-S	75.3 \pm 0.2	71.1 \pm 0.2	62.5 \pm 0.8	52.1 \pm 2.0	36.1 \pm 1.7	
	CCS	76.9\pm0.3	73.8\pm0.3	67.8\pm0.7	60.7 \pm 0.6	45.2 \pm 2.4	
	D2	75.1 \pm 0.5	71.2 \pm 0.2	67.8 \pm 0.9	61.1 \pm 1.4	44.3 \pm 2.6	
	TopoPrune	75.9 \pm 0.4	72.8 \pm 0.3	66.9 \pm 0.5	61.9\pm0.6	45.8\pm0.7	
ImageNet-1K (ResNet-50)							
<i>No Training Dynamics</i>	Random	69.8 \pm 0.5	68.4 \pm 0.5	65.1 \pm 0.4	61.9 \pm 0.5	52.5 \pm 0.6	
	Moderate	69.5 \pm 0.2	65.8 \pm 0.4	60.5 \pm 0.1	57.7 \pm 0.2	50.0 \pm 0.4	
	FDMat	70.8\pm0.3	68.7 \pm 0.5	65.5 \pm 0.7	62.0 \pm 0.3	51.9 \pm 0.3	
	TopoPrune (NLPS)	70.7 \pm 0.4	69.9\pm0.2	66.4\pm0.2	63.2\pm0.3	53.9\pm0.2	
<i>With Training Dynamics</i>	Moderate (AUM)	69.6 \pm 0.4	67.2 \pm 0.6	63.9 \pm 0.8	60.4 \pm 0.6	52.7 \pm 0.3	
	Forgetting	69.9 \pm 0.2	66.8 \pm 0.6	60.2 \pm 0.5	59.1 \pm 0.4	50.0 \pm 0.5	
	Glister	66.3 \pm 0.4	63.5 \pm 0.3	59.3 \pm 0.5	56.5 \pm 0.3	49.3 \pm 0.8	
	LCMat-S	69.8 \pm 0.4	67.5 \pm 0.5	62.2 \pm 0.3	59.7 \pm 0.5	48.8 \pm 0.6	
	CCS	70.1 \pm 0.5	69.1 \pm 0.3	65.7 \pm 0.3	62.6 \pm 0.6	55.2 \pm 0.7	
	D2	69.5 \pm 0.3	67.1 \pm 0.5	65.7 \pm 0.4	62.7 \pm 0.9	55.5 \pm 1.3	
	TopoPrune	70.8\pm0.2	69.5\pm0.2	66.2\pm0.1	63.1\pm0.3	56.1\pm0.2	

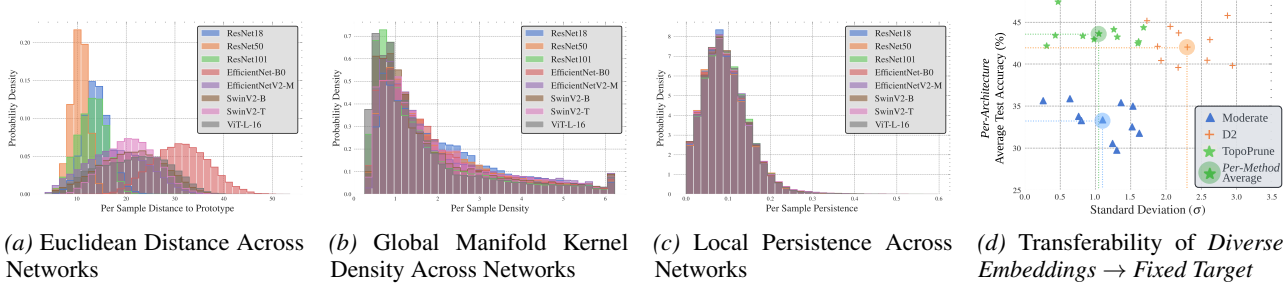


Figure 3. Topological metrics are more consistent across networks. Which translates directly to better coresnet performance. Metric distributions become progressively more uniform as we move from (a) unstable Euclidean distances, to (b) density estimation from global topological projection, and finally to (c) local persistence. This enhanced metric stability allows TopoPrune to consistently outperform geometry-based baselines (d), achieving both higher mean accuracy and lower standard deviation across 10 diverse architectures at a high pruning rate of 90% for CIFAR-100, where top left (low standard deviation and high accuracy) is best.

harana et al., 2024) uses a message-passing graph network while also incorporating AUM for mislabeled samples. All reported accuracies and standard deviations are computed over five independent training runs.

4.2. Performant and Stable Coresets with TopoPrune

Our experiments, detailed in Table 1, demonstrate that TopoPrune consistently yields higher-quality coresets than existing baselines across CIFAR-10, CIFAR-100, and ImageNet-1K. Specifically, TopoPrune (NLPS) outperforms all other training dynamic-free methods in the majority of pruning scenarios. Notably, this performance advantage scales with task difficulty. While competitive on simpler datasets, our method’s dominance becomes most pronounced on challenging ImageNet-1K benchmarks and at extreme pruning rates (e.g., 90%), consistently ranking as the top-performing method. Beyond accuracy, TopoPrune exhibits remarkable stability. As evidenced by the standard deviation metrics in Table 1, and validated via statistical significance testing in Section D.1, our approach delivers significantly higher precision compared to extrinsic geometric baselines. For instance, on ImageNet-1K at 90% pruning, TopoPrune reduces variance by up to $6.5 \times$ relative to the graph-based heuristics of D2. This stability is a practical asset, ensuring reliable data selection without needing to run multiple costly trials to mitigate the stochasticity of training from scratch.

4.3. Stability and Transferability Across Architectures

We investigate the limitations of geometric metrics across a wide range of network architectures, finding that stability and transferability increase dramatically as we move toward topology-based metrics. (1) *Metric Stability*: First, we analyze the Euclidean distance of samples to their class prototype. This metric proves highly inconsistent across architectures, demonstrating "geometric brittleness" (Fig. 3a).

In contrast, our topological metrics show remarkable stability. The global Density Score (Fig. 3b) improves uniformity, while the local Persistence Score (Fig. 3c) aligns almost perfectly across all tested architectures. (2) *Diverse Embeddings → Fixed Target*: Leveraging this stability, we evaluate transferability from diverse feature embeddings to a single target model. As detailed in Fig. 3d, TopoPrune consistently yields higher accuracy and lower standard deviation across diverse proxies (ResNet, EfficientNet, Swin, ViT, OpenCLIP) to train a fixed ResNet-18 target, significantly outperforming geometric baselines. Please see Appendix Table 10 for detailed values and Section A.2 for further theoretical justification. (3) *Fixed Embedding → Diverse Targets*: Finally, we validate transferring from a static feature embedding to diverse target models. Using a standard ResNet proxy to select coresets for training EfficientNet and Swin Transformers, we find that TopoPrune achieves performance competitive with, and in some cases exceeding, "Oracle" selection where the target model selects its own coresset (see Table 2). This confirms that topological importance derived from standard proxy embeddings are highly generalizable, allowing users to select a single, high-quality coresset effective for a wide range of downstream architectures.

Implications. The superior architectural transferability of our method has practical implications beyond the use of small proxy models (Coleman et al., 2020). It is a step towards the creation of reusable, model-agnostic coresets, where a dataset can be curated once with an efficient model and then used to train or benchmark a multitude of diverse, larger architectures. This approach aligns with recent work that uses topological measures, such as Betti numbers, to investigate and compare the complexity of embedding spaces across different networks (Suresh et al., 2024).

Table 2. Transferability of Fixed Embedding → Diverse Targets. We compare the "Oracle" performance (coreset selected from TopoPrune using the target model's own embeddings) against coresets selected from TopoPrune using smaller proxy model embeddings (ResNet-18 for CIFAR-100 and ResNet-50 for ImageNet-1k) to train a diverse range of models.

Pruning Rate (→)	80%			90%		
	Oracle	ResNet-18	Δ	Oracle	ResNet-18	Δ
CIFAR-100						
ResNet-50	57.0±0.6	56.1±0.7	-0.9	38.7±1.4	39.6±1.6	+0.9
EfficientNet-B0	55.0±2.1	54.4±1.4	-0.6	39.8±1.9	39.7±3.3	-0.1
SwinV2-T	38.1±0.7	39.9±0.9	+1.8	27.6±1.2	29.6±1.5	+2.0
Pruning Rate (→)	80%			90%		
ImageNet-1K						
EfficientNetV2-M	39.1±1.4	40.8±0.3	+1.7	35.9±0.3	37.1±1.3	+1.2
SwinV2-T	57.8±0.7	59.0±1.1	+1.2	38.3±3.4	38.0±4.1	-0.3
SwinV2-B	44.7±1.2	45.8±2.1	+1.1	44.4±2.1	45.1±1.1	+0.7

4.4. Stability to Noisy Feature Embeddings

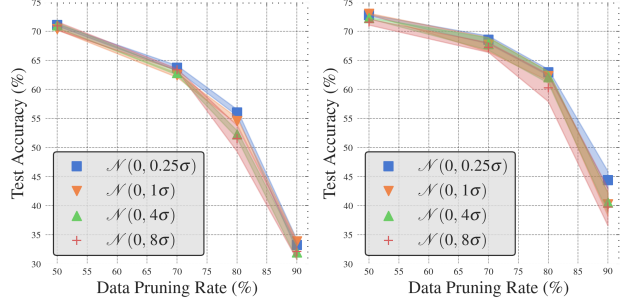
To evaluate the robustness of our method to perturbations in the latent space, we inject Gaussian noise into the penultimate layer embeddings of a ResNet-18 model on CIFAR-100. We compare TopoPrune against geometry-based baselines, Moderate (Xia et al., 2023) and D2 (Maharana et al., 2024), which are sensitive to such perturbations. "Noisy" versions of the feature embeddings are created by perturbing each sample's feature vector, $\mathbf{z} \in \mathbb{R}^D$. This is done by first computing the standard deviation of each sample's feature vector, $\sigma_{\mathbf{z}}$, then adding a noise vector $\epsilon \sim \mathcal{N}(0, \sigma_{\mathbf{z}})$ to the original features $\mathbf{z}' = \mathbf{z} + \epsilon$.

As shown in Fig. 4, TopoPrune demonstrates higher resilience to noise across all tested levels. While the performance of the baseline methods degrades with increased perturbation, our topological approach maintains high accuracy and stability. This robustness is particularly evident at high pruning rates, highlighting our method's ability to identify a stable coresset even in a noisy feature space. For detailed quantitative results, see Table 9 in the appendix.

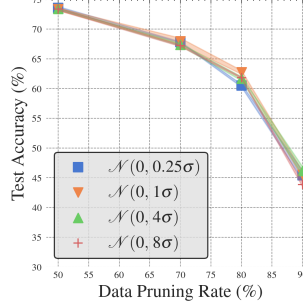
Implications. This robustness to noisy features indicates our method is not overly dependent on a perfectly optimized source model. This suggests that effective coresets could be generated using embeddings from models that are partially-trained, quantized for edge devices, or applied to slightly out-of-distribution data as similarly shown in (Turkes et al., 2022). This flexibility broadens the potential applicability of our approach to a wider range of practical scenarios.

5. Conclusion

In this work, we address the critical challenge of instability in geometric coresets selection methods, which arises from their reliance on extrinsic metrics. We present TopoPrune, a novel framework that overcomes this "geometric brittle-



(a) Moderate (Xia et al., 2023) (b) D2 (Maharana et al., 2024)



(c) TopoPrune (Ours)

Figure 4. Impact of noisy feature embeddings for Moderate, D2, and TopoPrune on CIFAR-100. (a) Moderate has decent precision (shown by the tightness of the shaded region) but lower accuracy on average. (b) D2 has higher accuracy but significantly looser precision, especially at high pruning rate and high ϵ -noise. (c) TopoPrune achieves both high accuracy and tighter standard deviation across all pruning rates and ϵ -noise.

ness" by leveraging topology to capture the data's intrinsic structure. Our dual-scale topological approach combines a global topology-aware manifold projection with a local importance score derived from differentiable persistent homology. TopoPrune exhibits several key advantages: (1) yields coresets with provably higher accuracy and stability, (2) is more stable across a wide range of network architectures, and (3) is highly robust to noisy feature embeddings.

The stability of TopoPrune makes it useful in practical applications. For the training of large foundational models, it curtails the "random seed lottery," de-risking the effects of instability by ensuring a consistently high-quality data subset. In automated pipelines, its more deterministic nature provides the auditability and reliability essential for building trustworthy, maintainable and safety-critical AI systems. By delivering both accuracy and stability, TopoPrune marks a step towards feasible and principled topology-based framework's for data-efficient learning.

Impact Statement

The research presented in this paper advances the understanding of deep learning by establishing differential persistent homology as a rigorous tool for probing the intrinsic structure of neural representations. By bridging global manifold geometry and local topological interactions, TopoPrune offers a novel lens for interpreting how deep models organize and separate data. Beyond its immediate application in efficient coresnet selection, this framework provides a robust, training-free mechanism for quantifying sample importance and filtering label noise. Ultimately, this work lays the foundation for future topological explainability tools, offering scalable insights into complex model dynamics while enabling high-performance training in resource-constrained environments.

Acknowledgements

This project was supported in part by the Purdue Center for Secure Microelectronics Ecosystem – CSME#210205 and the Center for the Co-Design of Cognitive Systems (CoCoSys), a DARPA-sponsored JUMP 2.0 center.

References

Bauer, U., Masood, T. B., Giunti, B., Houry, G., Kerber, M., and Rathod, A. Keeping it sparse: Computing persistent homology revisited. *ArXiv*, 2022.

Becht, E., McInnes, L., Healy, J., Dutertre, C.-A., Kwok, I., Ng, L. G., Ginhoux, F., and Newell, E. W. Dimensionality reduction for visualizing single-cell data using umap. *Nature Biotechnology*, 2018.

Birdal, T., Lou, A., Guibas, L., and Simsekli, U. Intrinsic dimension, persistent homology and generalization in neural networks. In *Advances in Neural Information Processing Systems*, 2021.

Boissonnat, J.-D. and Maria, C. The simplex tree: An efficient data structure for general simplicial complexes. *Algorithmica*, 2014.

Borsos, Z., Mutny, M., and Krause, A. Coresets via bilevel optimization for continual learning and streaming. *Advances in Neural Information Processing Systems*, 2020.

Botnan, M. B. and Lesnick, M. An introduction to multiparameter persistence. *ArXiv*, 2022.

Carriere, M., Chazal, F., Glisse, M., Ike, Y., Kannan, H., and Umeda, Y. Optimizing persistent homology based functions. In *International Conference on Machine Learning*. PMLR, 2021.

Carrière, M., Theveneau, M., and Lacombe, T. Diffeomorphic interpolation for efficient persistence-based topological optimization. In *Advances in Neural Information Processing Systems*, 2024.

Chazal, F., Cohen-Steiner, D., Guibas, L. J., Mémoli, F., and Oudot, S. Y. Gromov-hausdorff stable signatures for shapes using persistence. *Computer Graphics Forum*, 2009.

Chen, H., Chen, W., Mei, H., Liu, Z., Zhou, K., Chen, W., Gu, W., and Ma, K.-L. Visual abstraction and exploration of multi-class scatterplots. *IEEE Transactions on Visualization & Computer Graphics*, 2014.

Cho, Y., Shin, B., Kang, C., and Yun, C. Lightweight dataset pruning without full training via example difficulty and prediction uncertainty. In *International Conference on Machine Learning*, 2025.

Cohen-Steiner, D., Edelsbrunner, H., and Harer, J. Stability of persistence diagrams. In *Symposium on Computational Geometry*, 2005.

Coleman, C., Yeh, C., Mussmann, S., Mirzasoleiman, B., Bailis, P., Liang, P., Leskovec, J., and Zaharia, M. Selection via proxy: Efficient data selection for deep learning. In *International Conference on Learning Representations*, 2020.

de Bodt, C., Diaz-Papkovich, A., Bleher, M., Bunte, K., Coupette, C., Damrich, S., Sanmartin, E. F., Hamprecht, F. A., Horvát, E.-Á., Kohli, D., et al. Low-dimensional embeddings of high-dimensional data. *ArXiv*, 2025.

Dosovitskiy, A., Beyer, L., Kolesnikov, A., Weissenborn, D., Zhai, X., Unterthiner, T., Dehghani, M., Minderer, M., Heigold, G., Gelly, S., et al. An image is worth 16x16 words: Transformers for image recognition at scale. In *International Conference on Learning Representations*, 2021.

Edelsbrunner, H. and Harer, J. L. *Computational Topology: An Introduction*. American Mathematical Society, 2010.

Fel, T., Boutin, V., Béthune, L., Cadene, R., Moayeri, M., Andéol, L., Chalvidal, M., and Serre, T. A holistic approach to unifying automatic concept extraction and concept importance estimation. In *Advances in Neural Information Processing Systems*, 2023.

Fel, T., Béthune, L., Lampinen, A. K., Serre, T., and Hermann, K. Understanding visual feature reliance through the lens of complexity. In *Advances in Neural Information Processing Systems*, 2024.

Feldman, V. Does learning require memorization? a short tale about a long tail. In *ACM SIGACT Symposium on Theory of Computing*, 2020.

Feldman, V. and Zhang, C. What neural networks memorize and why: Discovering the long tail via influence estimation. *Advances in Neural Information Processing Systems*, 2020.

Garg, I. and Roy, K. Samples with low loss curvature improve data efficiency. In *IEEE/CVF Conference on Computer Vision and Pattern Recognition*, 2023.

Garg, I., Ravikumar, D., and Roy, K. Memorization through the lens of curvature of loss function around samples. In *International Conference on Machine Learning*, 2024.

Guo, C., Zhao, B., and Bai, Y. Deepcore: A comprehensive library for coresnet selection in deep learning. In *International Conference on Database and Expert Systems Applications*, pp. 181–195. Springer, 2022.

He, K., Zhang, X., Ren, S., and Sun, J. Deep residual learning for image recognition. In *IEEE/CVF Conference on Computer Vision and Pattern Recognition*, 2016.

He, M., Yang, S., Huang, T., and Zhao, B. Large-scale dataset pruning with dynamic uncertainty. In *IEEE/CVF Conference on Computer Vision and Pattern Recognition*, 2024.

He, Y., Xiao, L., and Zhou, J. T. You only condense once: Two rules for pruning condensed datasets. In *Advances in Neural Information Processing Systems*, 2023.

Jeon, H., Park, J., Shin, S., and Seo, J. Stop misusing t-sne and umap for visual analytics. *ArXiv*, 2025.

Killamsetty, K., Ramakrishnan, G., De, A., and Iyer, R. Grad-match: Gradient matching based data subset selection for efficient deep model training. In *International Conference on Machine Learning*, 2021a.

Killamsetty, K., Sivasubramanian, D., Ramakrishnan, G., and Iyer, R. Glister: Generalization based data subset selection for efficient and robust learning. In *AAAI Conference on Artificial Intelligence*, 2021b.

Lesnick, M. and Wright, M. Computing minimal presentations and bigraded betti numbers of 2-parameter persistent homology. *SIAM Journal on Applied Algebra and Geometry*, 2022.

Liu, Z., Hu, H., Lin, Y., Yao, Z., Xie, Z., Wei, Y., Ning, J., Cao, Y., Zhang, Z., Dong, L., et al. Swin transformer v2: Scaling up capacity and resolution. In *IEEE/CVF Conference on Computer Vision and Pattern Recognition*, 2022.

Loiseaux, D. and Schreiber, H. Multipers: Multiparameter Persistence for Machine Learning. *Journal of Open Source Software*, 9(103):6773, November 2024. ISSN 2475-9066. doi: 10.21105/joss.06773.

Loiseaux, D., Carrière, M., and Blumberg, A. A framework for fast and stable representations of multiparameter persistent homology decompositions. In *Advances in Neural Information Processing Systems*, 2023a.

Loiseaux, D., Scoccola, L., Carrière, M., Botnan, M. B., and Oudot, S. Stable vectorization of multiparameter persistent homology using signed barcodes as measures. *Advances in Neural Information Processing Systems*, 2023b.

Maharana, A., Yadav, P., and Bansal, M. D2 pruning: Message passing for balancing diversity & difficulty in data pruning. In *International Conference on Learning Representations*, 2024.

Maria, C., Dlotko, P., Rouvreau, V., and Glisse, M. Rips complex. In *GUDHI User and Reference Manual*. GUDHI Editorial Board, 3.11.0 edition, 2025.

McInnes, L., Healy, J., and Melville, J. Umap: Uniform manifold approximation and projection for dimension reduction. *ArXiv*, 2018a.

McInnes, L., Healy, J., Saul, N., and Grossberger, L. Umap: Uniform manifold approximation and projection. *The Journal of Open Source Software*, 3(29):861, 2018b.

Mindermann, S., Brauner, J. M., Razzak, M. T., Sharma, M., Kirsch, A., Xu, W., Höltgen, B., Gomez, A. N., Morisot, A., Farquhar, S., et al. Prioritized training on points that are learnable, worth learning, and not yet learnt. In *International Conference on Machine Learning*, 2022.

Mirzasoleiman, B., Bilmes, J. A., and Leskovec, J. Coresets for data-efficient training of machine learning models. In *International Conference on Machine Learning*, 2019.

Mishra, A. and Motta, F. C. Stability and machine learning applications of persistent homology using the delaunay-rips complex. *Frontiers in Applied Mathematics and Statistics*, 2023.

Moor, M., Horn, M., Rieck, B., and Borgwardt, K. Topological autoencoders. In *International Conference on Machine Learning*, 2020.

Mukherjee, S., Samaga, S. N., Xin, C., Oudot, S., and Dey, T. K. D-gril: End-to-end topological learning with 2-parameter persistence. *ArXiv*, 2024.

Nagaraj, M., Ravikumar, D., and Roy, K. Coresets from trajectories: Selecting data via correlation of loss differences. *Transactions on Machine Learning Research*, 2025.

Naitzat, G., Zhitnikov, A., and Lim, L.-H. Topology of deep neural networks. *Journal of Machine Learning Research*, 2020.

Otter, N., Porter, M. A., Tillmann, U., Grindrod, P., and Harrington, H. A. A roadmap for the computation of persistent homology. *EPJ Data Science*, 2017.

Oudot, S. *Persistence Theory: From Quiver Representations to Data Analysis*. Mathematical Surveys and Monographs. 2015. ISBN 9781470425456.

Papillon, M., Sanborn, S., Mathe, J., Cornelis, L., Bertics, A., Buracas, D., Lillemark, H. J., Shewmake, C., Dinc, F., Pennec, X., et al. Beyond euclid: an illustrated guide to modern machine learning with geometric, topological, and algebraic structures. *Machine Learning: Science and Technology*, 2025.

Paul, M., Ganguli, S., and Dziugaite, G. K. Deep learning on a data diet: Finding important examples early in training. *Advances in Neural Information Processing Systems*, 2021.

Pearson, K. Liii. on lines and planes of closest fit to systems of points in space. *The London, Edinburgh, and Dublin Philosophical Magazine and Journal of Science*, 1901.

Pleiss, G., Zhang, T., Elenberg, E., and Weinberger, K. Q. Identifying mislabeled data using the area under the margin ranking. *Advances in Neural Information Processing Systems*, 2020.

Pooladzandi, O., Davini, D., and Mirzaoleiman, B. Adaptive second order coresets for data-efficient machine learning. In *International Conference on Machine Learning*, 2022.

Radford, A., Kim, J. W., Hallacy, C., Ramesh, A., Goh, G., Agarwal, S., Sastry, G., Askell, A., Mishkin, P., Clark, J., Krueger, G., and Sutskever, I. Learning transferable visual models from natural language supervision. In *International Conference on Machine Learning*, 2021.

Schuhmann, C., Beaumont, R., Vencu, R., Gordon, C. W., Wightman, R., Cherti, M., Coombes, T., Katta, A., Mullis, C., Wortsman, M., Schramowski, P., Kundurthy, S. R., Crowson, K., Schmidt, L., Kaczmarczyk, R., and Jitsev, J. LAION-5b: An open large-scale dataset for training next generation image-text models. In *Advances in Neural Information Processing Systems Datasets and Benchmarks Track*, 2022.

Scoccola, L., Setlur, S., Loiseaux, D., Carrière, M., and Oudot, S. Differentiability and optimization of multiparameter persistent homology. In *International Conference on Machine Learning*, 2024.

Seifert, H. and Threlfall, W. *A textbook of topology*. Academic Press, 1980. ISBN 0-12-634850-2.

Shin, S., Bae, H., Shin, D., Joo, W., and Moon, I.-C. Loss-curvature matching for dataset selection and condensation. In *International Conference on Artificial Intelligence and Statistics*, 2023.

Suresh, S., Das, B., Abrol, V., and Roy, S. D. On characterizing the evolution of embedding space of neural networks using algebraic topology. *Pattern Recognition Letters*, 2024.

Swayamdipta, S., Schwartz, R., Lourie, N., Wang, Y., Hajishirzi, H., Smith, N. A., and Choi, Y. Dataset cartography: Mapping and diagnosing datasets with training dynamics. *ArXiv*, 2020.

Tan, H., Wu, S., Du, F., Chen, Y., Wang, Z., Wang, F., and Qi, X. Data pruning via moving-one-sample-out. In *Advances in Neural Information Processing Systems*, 2023.

Tan, M. and Le, Q. Efficientnet: Rethinking model scaling for convolutional neural networks. In *International Conference on Machine Learning*, 2019.

Tan, M. and Le, Q. Efficientnetv2: Smaller models and faster training. In *International Conference on Machine Learning*, 2021.

Toneva, M., Sordoni, A., des Combes, R. T., Trischler, A., Bengio, Y., and Gordon, G. J. An empirical study of example forgetting during deep neural network learning. In *International Conference on Learning Representations*, 2019.

Trofimov, I., Cherniavskii, D., Tulchinskii, E., Balabin, N., Burnaev, E., and Barannikov, S. Learning topology-preserving data representations. In *International Conference on Learning Representations*, 2023.

Turkes, R., Montufar, G. F., and Otter, N. On the effectiveness of persistent homology. *Advances in Neural Information Processing Systems*, 2022.

van der Maaten, L. and Hinton, G. Visualizing data using t-sne. *Journal of Machine Learning Research*, 2008.

Wang, Y., Huang, H., Rudin, C., and Shaposhnik, Y. Understanding how dimension reduction tools work: an empirical approach to deciphering t-sne, umap, trimap, and pacmap for data visualization. *Journal of Machine Learning Research*, 2021.

Xia, X., Liu, J., Yu, J., Shen, X., Han, B., and Liu, T. Moderate coresnet: A universal method of data selection for real-world data-efficient deep learning. In *International Conference on Learning Representations*, 2023.

Xiao, W., Chen, Y., Shan, Q., Wang, Y., and Su, J. Feature distribution matching by optimal transport for effective and robust coreset selection. *AAAI Conference on Artificial Intelligence*, 2024.

Xie, T., Zhu, J., Ma, G., Lin, M., Chen, W., Yang, W., and Liu, S. Structural-entropy-based sample selection for efficient and effective learning. In *International Conference on Learning Representations*, 2025.

Xiong, Z., Dalmasso, N., Sharma, S., Lecue, F., Magazzeni, D., Potluru, V. K., Balch, T., and Veloso, M. Fair wasserstein coresets. In *Advances in Neural Information Processing Systems*, 2024.

Yang, S., Cao, Z., Guo, S., Zhang, R., Luo, P., Zhang, S., and Nie, L. Mind the boundary: Coreset selection via reconstructing the decision boundary. In *International Conference on Machine Learning*, 2024.

Zheng, H., Liu, R., Lai, F., and Prakash, A. Coverage-centric coresset selection for high pruning rates. In *International Conference on Learning Representations*, 2023.

Zheng, H., Tsai, E., Lu, Y., Sun, J., Bartoldson, B. R., Kailkhura, B., and Prakash, A. ELFS: Label-free coresset selection with proxy training dynamics. In *International Conference on Learning Representations*, 2025.

Appendix

TABLE OF CONTENTS

A Conceptual Framework & Intuition	13
A.1 Overview of Simplicial Complexes and Persistent Homology	13
A.2 Theoretical Justification: On the Transferability of Topological vs. Euclidean Features	14
A.2.1 Instability of Euclidean Distances to Prototypes	15
A.2.2 Stability Guarantees for Persistent Homology	15
A.3 Topological Density and the Geometry of Sample Memorization	16
A.4 Illustrative Example of Coreset Construction	16
B Implementation & Computational Analysis	17
B.1 Comparative Analysis of Manifold Projection Techniques	17
B.1.1 Evaluation of Standard Linear and Non-linear Manifold Approximations	17
B.1.2 Evaluation of Deep Topological Autoencoders	17
B.2 TopoPrune Pseudocode	20
B.3 Computational Complexity Analysis	21
C Ablation Studies	22
C.1 Differentiable Persistence Optimization Steps	22
C.2 Sensitivity of Local Persistence (α) and Global Density (β)	22
C.3 Training-free Proxies of Area Under Margin (AUM) for Mislabel Detection	23
C.4 Sensitivity to UMAP Manifold Projection Hyperparameters	23
D Extended Empirical Results	23
D.1 Statistical Significance of Stability Improvements	23
D.2 Roadmap of Detailed Experimental Results	24

A. Conceptual Framework & Intuition

A.1. Overview of Simplicial Complexes and Persistent Homology

Persistent homology is used to characterize the topological variations in the shape of a finite metric space across multiple scales. At a high level, this can be described as the "birth" and "death" (persistence) of topological structures (defined by a homology group). The process begins by constructing a *simplicial complex*, a collection of points (0-simplices), edges (1-simplices), triangles (2-simplices), and their higher-dimensional counterparts that represents the data's structure (Boissonnat & Maria, 2014). To analyze how this structure changes with scale, a *filtration* is created (see Fig. 5a). This is a nested sequence of simplicial complexes, $K_{r_1} \subseteq K_{r_2} \subseteq \dots \subseteq K_{r_n}$, indexed by a non-decreasing scale parameter r . For each complex K_r in the filtration, we can compute its *homology groups*, $H_k(K_r)$, which are vector spaces that algebraically capture its k -dimensional features.

The rank of this group, known as the k -th *Betti number* ($\beta_k = \text{rank}(H_k(K_r))$), provides a count of these features: β_0 counts connected components, β_1 counts loops or tunnels, β_2 counts voids, and so on. These values are central to understanding the distinction between an object's *extrinsic* geometry and its *intrinsic* topological properties. A classic example which illustrates this difference is that of a coffee mug and a torus (donut). These two objects are topologically equivalent because they share the same Betti numbers (see Fig. 5b). Although their extrinsic geometries (including their shape, curvatures, and distances as embedded in 3D space are very different), their intrinsic topology is identical. This is because one can be continuously deformed into the other without tearing or gluing, preserving the single hole that defines them both.

Persistent homology is not wedged to any form of metric construction, and in fact you can do persistence on purely abstract simplicial complexes and any filtration on it. However, for the purposes of our application, we apply this to a point cloud $P = \{\mathbf{x}_i\}$ using the common method of building a filtration with the *Vietoris-Rips (VR) complex* (see Fig. 5c). For a given scale $r \geq 0$, the complex $VR(P, r)$ contains all simplices $\sigma \subseteq P$ such that the Euclidean distance between any two

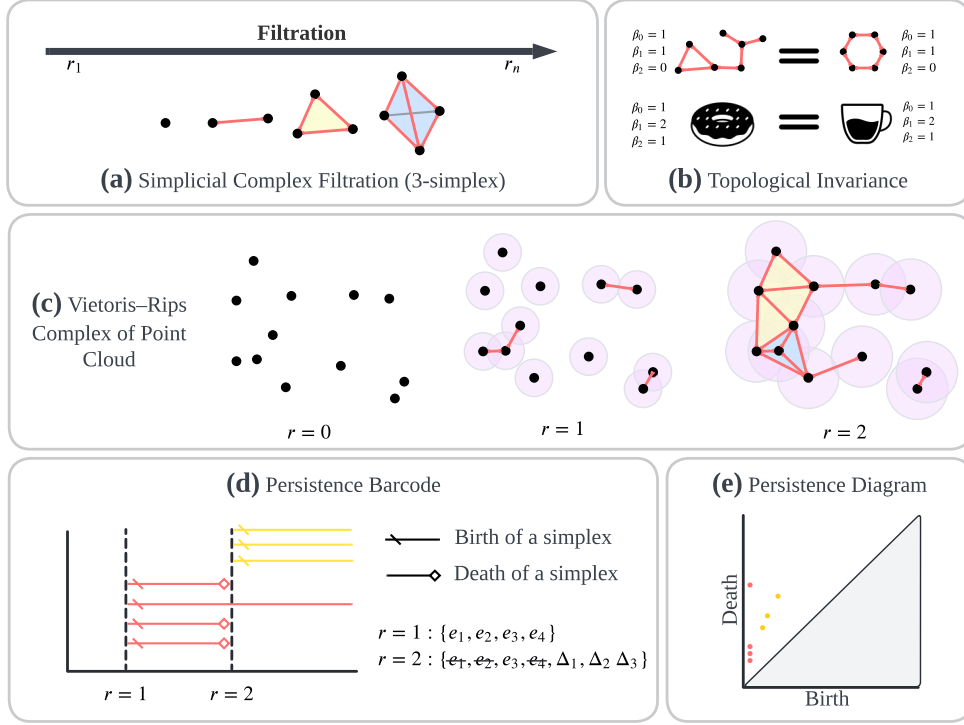


Figure 5. Overview of Simplicial Complexes and Persistent Homology

points in σ is at most $2r$. As r increases, simplices are added to the complex, causing new components to merge with older components. *Persistent homology tracks the birth and death of these topological features throughout the filtration.* The inclusion map $K_{r_i} \hookrightarrow K_{r_j}$ for $r_i \leq r_j$ induces a homomorphism between the homology groups, $H_k(K_{r_i}) \rightarrow H_k(K_{r_j})$. A feature is said to be "born" at a scale r_{birth} when it first appears and "dies" at a scale r_{death} when it merges with an older feature visualized by the persistence barcode (Fig. 5d).

Definition A.1 (Vietoris-Rips Filtration). *For a point cloud $P \subset \mathbb{R}^n$ and a scale parameter $r \geq 0$, the Vietoris-Rips complex $VR(P, r)$ is the simplicial complex whose vertices are the points in P and whose simplices are all finite subsets of P with a diameter of at most $2r$. A filtration is the nested sequence of complexes $\{VR(P, r)\}_{r \geq 0}$.*

The output of this process is summarized in a *persistence diagram* $Dgm(P)$, a multiset of points in the plane where each point corresponds to a single topological feature plotted at its $(\text{birth}, \text{death}) \rightarrow (b, d)$ coordinates (see Fig. 5e). The *persistence* of a feature is defined as its lifespan, $d - b$. Points in the diagram that are further from the diagonal line $y = x$ represent robust, structurally significant features of the data, while points close to the diagonal are interpreted as topological noise with short lifespans. This provides a stable, multi-scale signature of the data's underlying shape.

Definition A.2 (Persistence Diagram). *Applying the homology functor $H_k(\cdot)$ (for a fixed dimension k , e.g., $k = 0$ for connected components) to a filtration yields a set of birth-death pairs (b, d) representing the scales at which topological features appear and disappear. This multiset of pairs is the persistence diagram, denoted $Dgm(P)$. The persistence of a feature (b, d) is defined as $d - b$.*

Please note that for clarity and ease of visualization in this overview section, we present the 1-parameter persistence analysis. It is important to note, however, that our method, TopoPrune, employs a multi-parameter persistence module, which is more complex to visualize but provides a richer description of the data's topology.

A.2. Theoretical Justification: On the Transferability of Topological vs. Euclidean Features

We provide a formal argument for the superior transferability of topological features derived from persistent homology over traditional Euclidean metrics across different neural network architectures. We demonstrate that the stability guarantees inherent to persistent homology ensure that its output is robust to the geometric variations common between different

network embeddings. Conversely, we show that Euclidean-based metrics, such as the distance to a class prototype, are inherently sensitive to these variations (Papillon et al., 2025).

Preliminaries and Notation. Let X be the input data space and $Y = \{1, \dots, K\}$ be the set of K class labels. A neural network architecture is a function $f : X \rightarrow \mathbb{R}^n$ that maps input data to an n -dimensional embedding space. Let f_A and f_B denote two distinct network architectures (e.g., ResNet18 and ViT-L-16). The outputs of these networks for the entire dataset X are the point clouds $X_A = f_A(X)$ and $X_B = f_B(X)$ in their respective embedding spaces. We equip these embedding spaces with a standard Euclidean metric, d_E .

Definition A.3 (Bottleneck Distance). *The similarity between two persistence diagrams Dgm_1 and Dgm_2 is measured by the bottleneck distance $d_B(Dgm_1, Dgm_2)$, defined as the infimum over all bijections $\eta : Dgm_1 \rightarrow Dgm_2$ of the supremum of distances between matched points, where $p \in Dgm$ represents a point in the persistence diagram representing its birth and death pair $p = (b, d)$:*

$$d_B(Dgm_1, Dgm_2) = \inf_{\eta} \sup_{p \in Dgm_1} \|p - \eta(p)\|_{\infty}$$

Definition A.4 (Gromov-Hausdorff Distance). *The distance between two metric spaces (M) equipped with a distance function (d) ; (M_1, d_1) and (M_2, d_2) is measured by the Gromov-Hausdorff distance $d_{GH}(M_1, M_2)$, which is the infimum of distances over all possible isometric embeddings into a common metric space. It quantifies the “metric dissimilarity” of two spaces.*

A.2.1. INSTABILITY OF EUCLIDEAN DISTANCES TO PROTOTYPES

We now formalize the lack of such stability for Euclidean distances.

Definition A.5 (Class Prototype and Distance Distribution). *For an embedding $f(X)$ and a class $k \in Y$, the class prototype (centroid) is $c_k = \frac{1}{|X_k|} \sum_{x \in X_k} f(x)$, where X_k are the samples of class k . The set of distances to the prototype is $S_k(f) = \{d_E(f(x), c_k) \mid \text{label}(x) = k\}$. Let $P(S_k(f))$ be the probability distribution of these distances.*

Proposition A.6 (Sensitivity to Scaling). *Let f_A be a network embedding. Consider a new embedding f_B defined by a simple isotropic scaling transformation, $f_B(x) = \alpha f_A(x)$ for some scalar $\alpha > 0, \alpha \neq 1$. Then the distribution of distances to the prototype is scaled accordingly: $P(S_k(f_B)) = \alpha P(S_k(f_A))$.*

Proof. The new class prototype c'_k under the embedding f_B is:

$$c'_k = \frac{1}{|X_k|} \sum_{x \in X_k} f_B(x) = \frac{1}{|X_k|} \sum_{x \in X_k} \alpha f_A(x) = \alpha \left(\frac{1}{|X_k|} \sum_{x \in X_k} f_A(x) \right) = \alpha c_k$$

The distance for any sample x of class k to the new prototype is:

$$\begin{aligned} d_E(f_B(x), c'_k) &= d_E(\alpha f_A(x), \alpha c_k) \\ &= \|\alpha f_A(x) - \alpha c_k\|_2 \\ &= |\alpha| \cdot \|f_A(x) - c_k\|_2 = \alpha \cdot d_E(f_A(x), c_k) \end{aligned}$$

Thus, every distance value in the set $S_k(f_A)$ is multiplied by α to obtain the set $S_k(f_B)$. The probability distribution of these distances is therefore a scaled version of the original. \square

A.2.2. STABILITY GUARANTEES FOR PERSISTENT HOMOLOGY

The transferability of persistence-based features is a direct consequence of the fundamental stability theorems of topological data analysis.

Proposition A.7 (Invariance and Stability of Persistent Homology).

1. **Isometry Invariance** (Edelsbrunner & Harer, 2010): *Let $P \subset \mathbb{R}^n$ be a point cloud and $g : \mathbb{R}^n \rightarrow \mathbb{R}^n$ be a Euclidean isometry (translation, rotation, reflection). Then, the persistence diagram is unchanged: $Dgm(P) = Dgm(g(P))$.*

2. **Stability** (Chazal et al., 2009; Cohen-Steiner et al., 2005): Let X_A and X_B be two point clouds in \mathbb{R}^n . The bottleneck distance between their respective persistence diagrams is bounded by the Gromov-Hausdorff distance between their metric spaces:

$$d_B(Dgm(X_A), Dgm(X_B)) \leq d_{GH}((X_A, d_E), (X_B, d_E))$$

Remark. (1) An isometry g preserves all pairwise Euclidean distances. Since the Vietoris-Rips filtration is constructed based solely on these distances, the filtration $\{VR(P, r)\}_{r \geq 0}$ is identical to $\{VR(g(P), r)\}_{r \geq 0}$. Applying the homology functor to identical filtrations yields identical persistence diagrams. (2) The proof is a cornerstone result in topological data analysis. It formalizes the intuition that if two spaces are metrically similar (a small d_{GH}), their topological features as captured by persistence homology must also be similar (a small d_B).

A.3. Topological Density and the Geometry of Sample Memorization

We qualitatively examine the link between the intra-class density of our projected manifold and the established notion of sample memorization (Feldman, 2020; Feldman & Zhang, 2020), measured via the input curvature score (Garg et al., 2024). Our findings reveal a clear correspondence: *high-density*, prototypical samples consistently exhibit *low input curvature* (characteristic of un-memorized examples), while *low-density*, atypical samples show *high input curvature* (a key indicator of memorization). This alignment demonstrates that our topological manifold projection effectively preserves the global structure that distinguishes prototypical from atypical samples.



Figure 6. **Prototypical Samples:** Top-10 lowest curvature samples (left) vs. highest density samples (right) of the same class, for five CIFAR-100 classes.

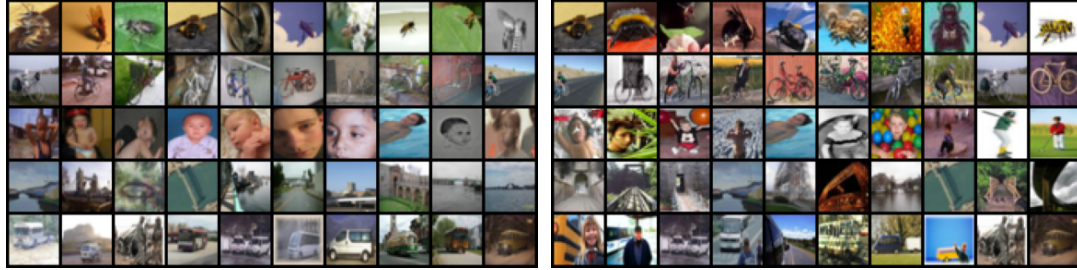


Figure 7. **Atypical Samples:** Top-10 highest curvature samples (left) vs. lowest density samples (right) of the same class, for five CIFAR-100 classes.

A.4. Illustrative Example of Coreset Construction

Qualitative visualization of TopoPrune at various pruning rates (70%, 50%, 30%, 20% and 10%) for the "butterfly" class in CIFAR-100 (see Fig. 8). The visualization reveals a high variance in Persistence Scores within localized regions of the class manifold, demonstrating the method's sensitivity to fine-grained local structures and its ability to distinguish between nearby samples. Despite this focus on local complexity, the final coresets remain density-preserving, with their overall distribution closely matching that of the full dataset. This illustrates how TopoPrune successfully balances the selection of topologically critical local samples with the preservation of the global data structure.

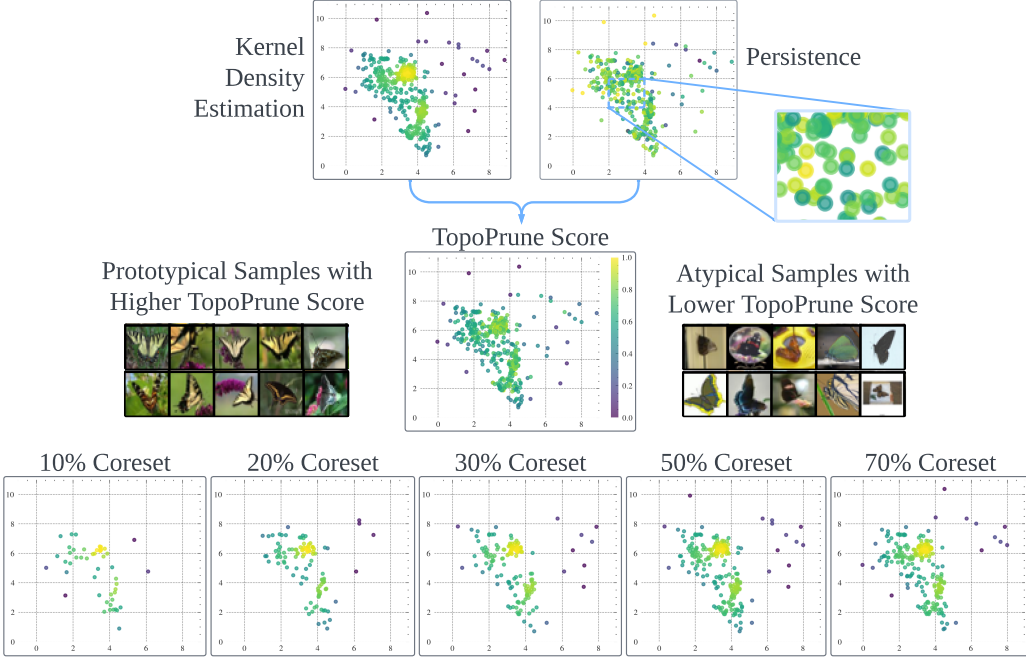


Figure 8. TopoPrune for "butterfly" class in CIFAR-100.

B. Implementation & Computational Analysis

B.1. Comparative Analysis of Manifold Projection Techniques

Our global manifold projection is critical for achieving metric stability across diverse neural network architectures. While high-dimensional embeddings may vary in their extrinsic geometry, they share a common intrinsic topology. UMAP leverages this shared structure to construct a new, low-dimensional manifold that is not only topologically faithful but also geometrically standardized. A key consequence of this process is that the resulting low-dimensional embeddings are *density-preserving* across architectures. This standardization ensures that the global density score, a core component of our sample importance calculation, is a stable and reliable metric regardless of the source network.

B.1.1. EVALUATION OF STANDARD LINEAR AND NON-LINEAR MANIFOLD APPROXIMATIONS

To further elaborate the standardization of topology-based manifold approximation and projection across perturbations in the embedding space we look at correlation (Fig. 9) and distributions (Fig. 10) of per-sample distance to prototypes across different manifold projection and feature reduction techniques (a) PCA (Pearson, 1901), (b) t-SNE (van der Maaten & Hinton, 2008) (c) PaCMAP (Wang et al., 2021) and (d) UMAP (McInnes et al., 2018a). We see that the topology-based methods, UMAP and PaCMAP, demonstrate significantly higher correlation and thus better transferability across architectures compared to linear PCA or the more locally-focused t-SNE. Notably, UMAP exhibits slightly superior transferability over PaCMAP, reinforcing its selection for our framework. This high correlation between smaller models (e.g., ResNet-18) and larger models is particularly valuable, as it validates the use of computationally inexpensive networks to generate manifold embeddings that remain effective for data selection on much larger models.

B.1.2. EVALUATION OF DEEP TOPOLOGICAL AUTOENCODERS

We also considered Topological Auto-Encoders (TopoAE) (Moor et al., 2020) and Regularized TDA (RTD) (Trofimov et al., 2023) for our manifold embedding. While these methods are powerful for preserving global topology, we chose UMAP for computational efficiency, domain suitability, and alignment with coresnet selection goals.

Computational cost and empirical validation. TopoPrune aims to be a lightweight, training-free method applicable to frozen features, a requirement UMAP fits perfectly. In contrast, training a topological autoencoder is computationally prohibitive for preprocessing; training RTD on CIFAR-100 takes \sim 8 hours compared to UMAP's \sim 22 seconds, representing

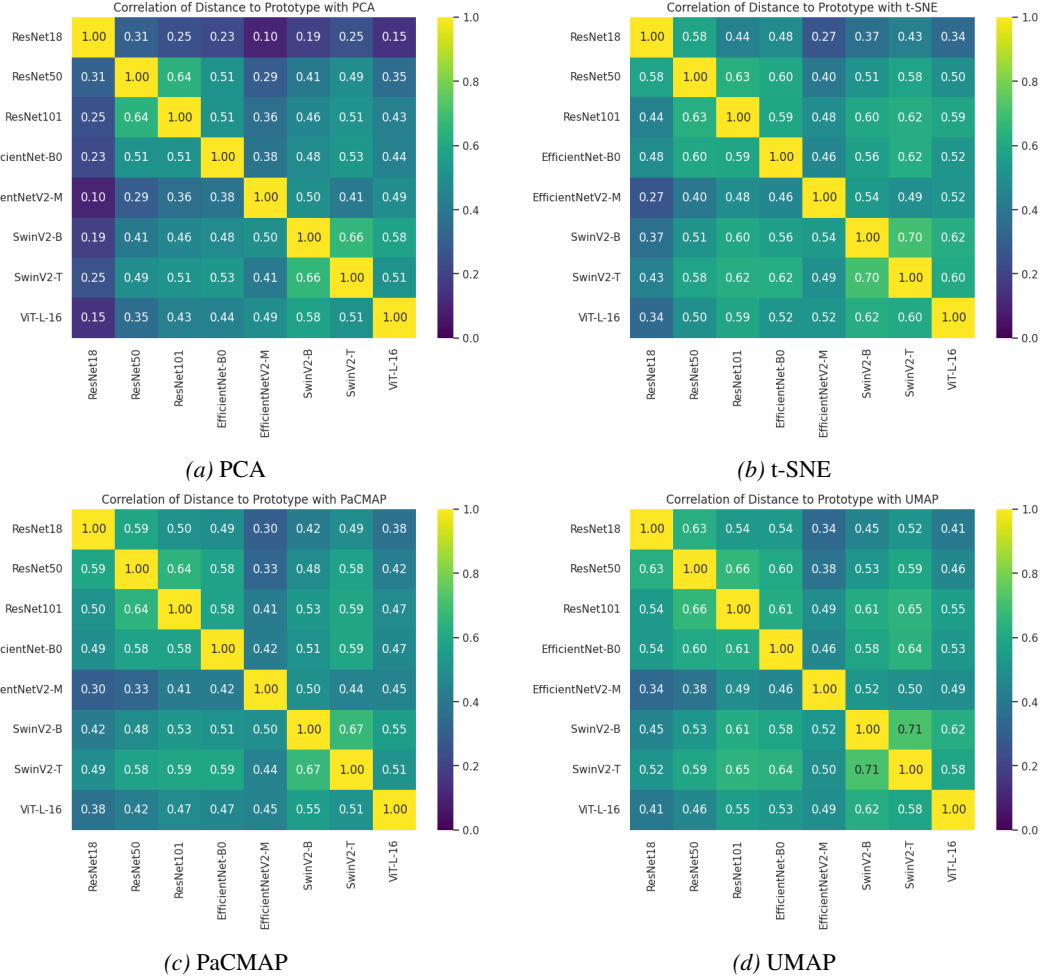


Figure 9. Correlation of per-sample distance to prototype across different architectures when applying different linear and non-linear manifold projection techniques.

a speedup of $> 1000\times$ (see Table 3a). To empirically validate our choice, we trained both TopoAE and RTD models on CIFAR-10/100 and used their embeddings as a replacement for UMAP in our pipeline. As shown in Table 3b, UMAP consistently yields superior or comparable accuracy without this massive training overhead.

Domain suitability and structural alignment. The observed drop in coresnet accuracy when using topological autoencoders likely stems from a fundamental misalignment of objectives. First, regarding latent space quality, TopoAE struggles to produce clean, separated representations for complex datasets. As noted in the TopoAE paper itself, CIFAR-10 is "challenging to embed... in a purely unsupervised manner" (Section 5.2.2 in Moor et al. (2020)), often resulting in latent spaces where classes are homogeneously mixed rather than cleanly separated (see Figure 4 in Moor et al. (2020)). This lack of separation severely hampers the effectiveness of our per-class density estimation, contrasting with the distinct cluster delineation achieved by UMAP. Furthermore, this issue is exacerbated because methods like TopoAE and RTD prioritize preserving global structural similarity (e.g., maintaining relative distances between distinct mammoth "head" and "foot" clusters as shown in Figure 1 in Trofimov et al. (2023)). While this global constraint is valuable for visualization, it is less relevant for coresnet selection, where we partition the data into class-based manifolds.

In summary, while topological autoencoders are robust tools for manifold learning, UMAP provides a more efficient, domain-appropriate, and higher-performing foundation for our specific multi-scale framework. We encourage future work exploring topological autoencoders that flexibly balance global and local structural priorities, specifically optimized for the task of point-cloud sparsification.

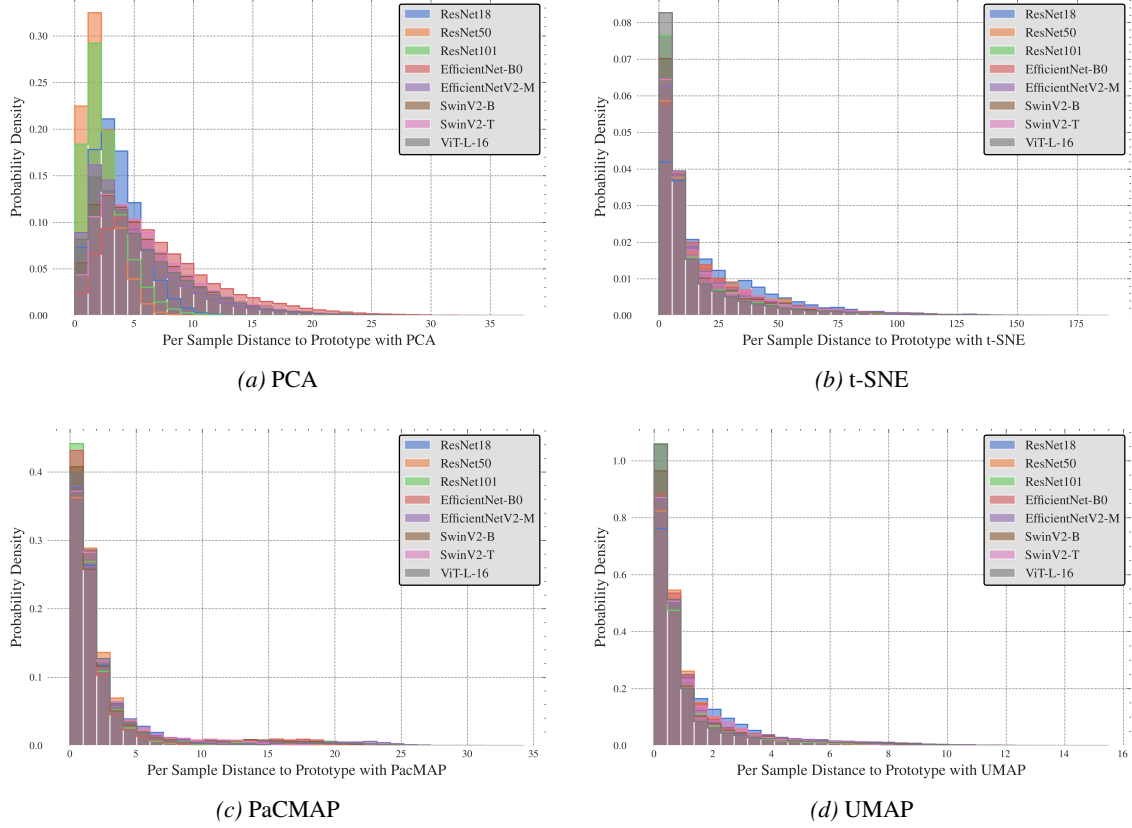


Figure 10. Distribution of per-sample distance to prototype across different architectures when applying different linear and non-linear manifold projection techniques.

Table 3. Throughput and accuracy when using Topological autoencoders. (a) Topological autoencoders require costly training vs. UMAP’s algorithmic projection. (b) Substituting UMAP with TopoAE or RTD for the global manifold embedding shows performance degradation.

Method	CIFAR-10	CIFAR-100
TopoAE (Moor et al., 2020)	14,847.79	15,248.11
RTD (Trofimov et al., 2023)	26,622.89	28,661.29
UMAP (McInnes et al., 2018a)	22.42	22.74

(a) Latency (s)

Method	CIFAR-10	CIFAR-100
TopoAE (Moor et al., 2020)	75.0 ± 0.3	41.2 ± 1.0
RTD (Trofimov et al., 2023)	78.0 ± 1.7	46.4 ± 0.4
UMAP (McInnes et al., 2018a)	82.1 ± 0.3	45.8 ± 0.7

(b) Accuracy at 90% Pruning Rate (Avg. over 3 runs)

B.2. TopoPrune Pseudocode

Algorithm 1 Coreset Selection with TopoPrune

Input: Dataset $\mathcal{D} = \{(x_i, y_i)\}_{i=1}^N$, Penultimate Layer Encoder h_θ , Pruning Rate p , Mislabel Ratio γ , Weights α, β , Persistence Optimization Steps T

Callables: UMAP, KDE, KNN

▷ see Hyperparameters in Table 13

Output: Selected Indices \mathcal{S}

Dual-Scale Topological Scoring

Extract embeddings: $Z \leftarrow h_\theta(X)$
 Global manifold projection: $Y \leftarrow \text{UMAP}(Z)$
 Initialize score vectors $S_{pers}, S_{dens} \leftarrow \mathbf{0}^N$
for each class $c \in \{1, \dots, C\}$ **do**
 Get indices $\mathcal{I}_c \leftarrow \{i \mid y_i = c\}$ and subset $Y_c \leftarrow Y[\mathcal{I}_c]$
 $S_{dens}[\mathcal{I}_c] \leftarrow \text{KDE}(Y_c)$ ▷ Global Density Score
 Initialize optimizable inputs $Y'_c \leftarrow Y_c$
 for $t = 1$ **to** T **do**
 Compute Hilbert decomposition signed measure: $\mu_{H_1(VR_{Y'_c}, \hat{f})}^{Hil}$
 Compute topological loss: $\mathcal{L}_{pers}(Y'_c) \leftarrow \text{OT}(\mu_{H_1(VR_{Y'_c}, \hat{f})}^{Hil}, \mathbf{0})$
 Update coordinates: $Y'_c \leftarrow Y'_c + \eta \nabla_{Y'_c} \mathcal{L}_{pers}$
 end for
 $S_{pers}[\mathcal{I}_c] \leftarrow \|Y_c - Y'_c\|_2$ ▷ Local Persistence Score
end for

Mislabel Detection and Filtering

if method is NLPS **then**
 for each sample $i \in \{1, \dots, N\}$ **do**
 Compute k nearest neighbors: $\mathcal{N}_k(z_i) \leftarrow \text{KNN}(Z)$
 Count mismatched neighbors: $m_i \leftarrow \sum_{j \in \mathcal{N}_k(z_i)} \mathbb{I}(y_j \neq y_i)$
 Compute label purity ratio: $S_{mis}^{(i)} \leftarrow m_i/k$ ▷ Training-Free
 end for
else if method is AUM **then**
 Grab precomputed score: $S_{mis} \leftarrow \text{AUM}(Z)$ ▷ with Training Dynamics
end if
 Identify mislabeled sample indices: $\mathcal{I}_{mis} \leftarrow \text{TopK}(S_{mis}, \gamma \cdot N)$
 Define clean candidate set: $\mathcal{D}_{clean} \leftarrow \mathcal{D} \setminus \mathcal{I}_{mis}$

Stratified Sampling on Unified Score

$S_{unified}^{(i)} \leftarrow \alpha \cdot S_{pers}^{(i)} + \beta \cdot S_{dens}^{(i)}$
 $\mathcal{S} \leftarrow \text{StratifiedSample}(\mathcal{D}_{clean}, S_{unified}, p)$ ▷ see Algorithm 1 in Zheng et al. (2023)
return \mathcal{S}

B.3. Computational Complexity Analysis

Theoretical Complexity Relative to Geometric Baselines. Our analysis follows the framework for evaluation of coresets selection complexity in [Nagaraj et al. \(2025\)](#). The core computational overhead of TopoPrune stems from the local topological optimization. However, we maintain tractability by leveraging efficient reductions of multi-parameter persistence.

- Crucially, we utilize the Hilbert decomposition signed measure, which *reduces the multi-parameter problem to one-parameter persistence slices along a grid*. As detailed in Appendix D.1 of [Loiseaux et al. \(2023b\)](#), for a 2-parameter filtration (Rips + Density) on a grid of size m , the algorithm performs m runs of a 1-parameter persistence optimization.
- Consequently, the persistent homology optimization cost is equivalent to that of a 1-parameter optimization on N_c points. While the theoretical worst-case for persistence is cubic ([Lesnick & Wright, 2022](#)), in the 1-parameter persistence case the computation is empirically linear ([Bauer et al., 2022](#)).
- Furthermore, computing the gradient of the loss $\mathcal{L}_{\text{pers}}$ (Eq. (3)) simplifies to summing feature persistences (see Corollary E.2 in [Scoccola et al. \(2024\)](#)). This operation is bounded by a constant K derived from the simplicial complex \mathcal{K} , making the backward pass $\mathcal{O}(K)$. Thus, a single local optimization cost is strictly $\mathcal{O}(m \cdot N_c \log N_c)$.

Table 4. Complexity analysis of geometry-based methods. N is the dataset size with C classes, $N_c \approx N/C$ samples per class, d dimension, and k neighbors. For TopoPrune, cost is dominated by T optimization steps and m grid resolution.

	Computational Complexity	Explanation
Moderate (Xia et al., 2023)	$\mathcal{O}(Nd) + C * \mathcal{O}(N_c \log N_c)$	Distance calc. (Nd) + Prototype sorting
D2 (Maharana et al., 2024)	$\mathcal{O}(Nkd) + \mathcal{O}(T \cdot Nk)$	kNN graph (Nkd) + Message passing
TopoPrune	$\mathcal{O}(N \log N) + C * \mathcal{O}(Tm \cdot N_c \log N_c)$	Global UMAP + Local persistence

Empirical Wall-Clock Analysis. We benchmarked the latency and resource utilization of TopoPrune against baselines on an AMD EPYC 7502 (32-Core) CPU. Despite exhibiting higher latency, our analysis reveals that TopoPrune significantly under-utilizes available hardware (16% utilization vs. 82% for baselines). This indicates an implementation-specific bottleneck rather than a fundamental algorithmic flaw, as our topological backend (`multipers`) currently lacks support for multi-processing and GPU acceleration. We anticipate that as topology libraries mature, this wall-clock gap will close significantly. Regardless of current implementation constraints, TopoPrune offers a superior cost-benefit profile for high-stakes data selection due to the following reasons. (1) TopoPrune is orders of magnitude faster than "training-dynamic" coresets methods (e.g., Glister, Forgetting), which require training a proxy model from scratch (hours of compute) compared to our probe of frozen embeddings (minutes). (2) Unlike fast geometric heuristics (e.g., D2, Moderate) which suffer from high variance and lower precision (as shown in [Table 1](#)), TopoPrune accepts a higher upfront computational cost to guarantee a stable, high-fidelity coresset. This eliminates the need for repeated selection runs to mitigate randomness.

TopoPrune remains tractable because it employs a construction that reduces the complex 2-parameter persistence problem to a sequence of m standard 1-parameter calculations. By applying this optimization per-class (where N_c is relatively small) and utilizing this efficient reduction strategy, we avoid the prohibitive costs typically associated with multiparameter topology. As topological software infrastructure improves, we expect TopoPrune to offer the superior stability of topological methods with negligible latency trade-offs.

C. Ablation Studies

C.1. Differentiable Persistence Optimization Steps

We investigate the impact of the number of optimization steps for multi-parameter persistent homology (see Fig. 11). The number of required persistence optimization steps is inversely correlated with the final coresset size. When selecting a large coresset (e.g., at a 30% pruning rate), the selection process is robust, and even a few optimization steps (1-2) suffice to identify a high-quality subset. However, at high pruning rates (e.g., 90%), the task of distinguishing the most crucial samples becomes more sensitive, necessitating a greater number of optimization steps (≥ 6) to allow the point positions to converge and accurately reveal the most structurally important examples.

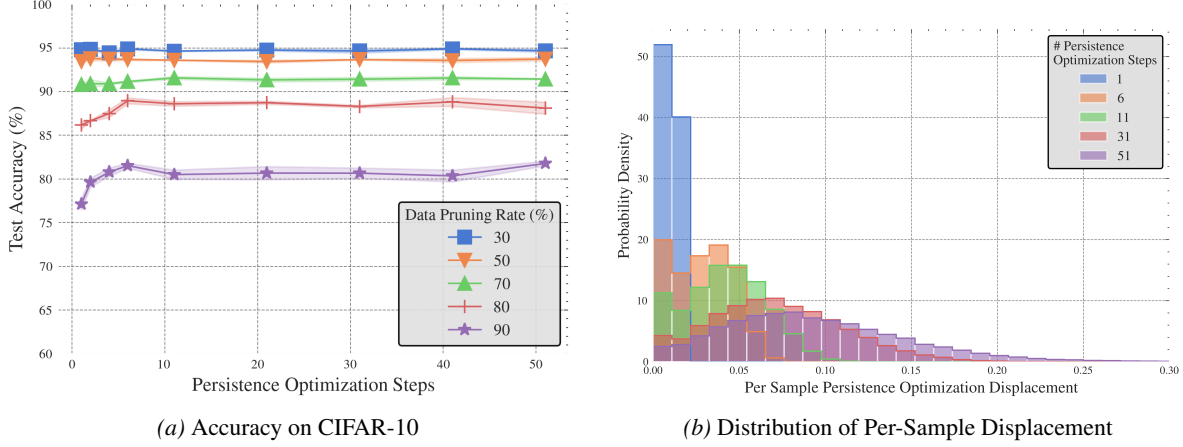


Figure 11. Smaller coressets have a lower margin for error, as the importance of each selected sample is magnified. Consequently, more optimization steps are needed to precisely distinguish the most critical samples. In contrast, larger coressets are more forgiving, requiring fewer steps to achieve a high-quality result.

C.2. Sensitivity of Local Persistence (α) and Global Density (β)

We investigate the impact of the hyperparameters α and β from Eq. (5), which balance the influence of our global density and local persistence scores (see Fig. 12). Our analysis reveals that while the coresset quality is generally stable across a range of (α, β) values, a combination of both metrics consistently yields the best performance. Although using either density or persistence alone provides a reasonable baseline, combining them is particularly crucial at high pruning rates (e.g., 90%), where a balanced score improves accuracy by up to 5.4% over using either metric in isolation. This demonstrates that both global and local topology are vital for optimal selection and justifies our use of a fixed and balanced configuration set at (50/50) across all experiments, minimizing the need for extensive hyperparameter tuning.

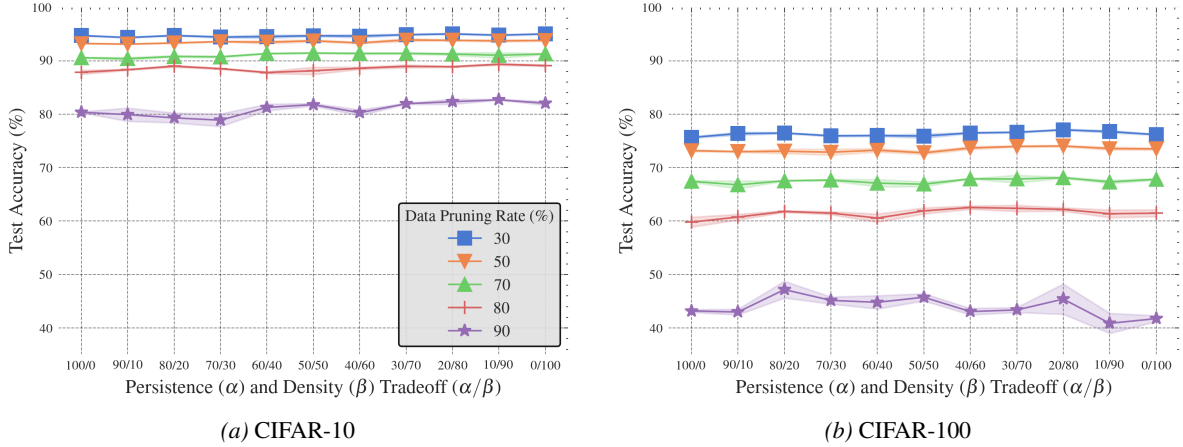


Figure 12. Topology hyperparameters across all ranges of data pruning rates for both (a) CIFAR-10 and (b) CIFAR-100.

C.3. Training-free Proxies of Area Under Margin (AUM) for Mislabel Detection

We evaluate several training-free methods to serve as a proxy for Area Under the Margin (AUM). These proxies identify potentially noisy samples using different geometric criteria, ranging from culling samples based on their *Distance* to the class prototype, to using an *Adjacent Distance* ratio to remove points closer to another class's prototype. Other heuristics include culling samples with the lowest *Density* score, or using our proposed *Neighborhood Label Purity Score (NLPS)*, which identifies points in mixed-label regions by calculating the fraction of same-label nearest neighbors (from 20 nearest neighbors). Our results show that NLPS provides the highest coresnet accuracy among all training-free proxies, with its advantage being most pronounced at high data pruning rates. While it does not fully match the performance of using the true AUM, NLPS serves as a simple and effective training-free proxy.

Table 6. Training-free proxies for Area Under Margin (AUM) (Pleiss et al., 2020) on CIFAR-100. We see that Neighborhood Label Purity Score (NLPS) performs closest to AUM.

Pruning Rate (\rightarrow)	30%	50%	70%	80%	90%
Distance	75.4 \pm 0.4	71.3 \pm 0.3	63.2 \pm 0.1	56.1 \pm 0.6	37.8 \pm 0.3
Adjacent Distance	75.5 \pm 0.3	71.8 \pm 0.2	62.8 \pm 1.0	57.1 \pm 0.3	38.1 \pm 1.5
Density	75.6 \pm 0.1	71.4 \pm 0.2	64.3 \pm 0.3	52.4 \pm 0.3	38.0 \pm 0.7
NLPS	75.6\pm0.2	71.9\pm0.2	65.3\pm0.4	56.7\pm0.4	41.6\pm1.0
AUM	75.9 \pm 0.4	72.8 \pm 0.3	66.9 \pm 0.5	61.9 \pm 0.6	45.7 \pm 0.7

C.4. Sensitivity to UMAP Manifold Projection Hyperparameters

To establish the robustness of the global manifold embedding stage of TopoPrune, we conducted a comprehensive hyperparameter sweep of UMAP. We specifically investigate two critical parameters: (1) *n_neighbors*, which controls the balance between local and global geometric preservation, and (2) *min_dist*, which governs how tightly samples are packed in the low-dimensional manifold. The results in Table 7 indicate that our selection of *n_neighbors*=15 and *min_dist*=0.1 provides a strong balance of high accuracy and low variance.

Table 7. TopoPrune sensitivity to UMAP hyperparameters. (a) accuracy on CIFAR-100 (90% pruning rate) and (b) relative change to default configuration when modulating *n_neighbors* and *min_dist* UMAP hyperparameters.

n_neighbors					
min_dist	5	15	50	100	Avg. over Rows
0.05	43.9 \pm 2.2	43.0 \pm 0.9	44.4 \pm 1.7	44.9 \pm 1.6	44.1 \pm 1.6
0.1	43.1 \pm 1.8	45.8\pm0.7	45.7 \pm 0.8	43.6 \pm 0.7	44.6 \pm 0.9
0.5	46.2 \pm 1.0	43.8 \pm 0.7	44.3 \pm 2.2	43.9 \pm 0.4	44.6 \pm 1.0
1.0	44.3 \pm 0.9	45.4 \pm 0.6	45.0 \pm 1.1	43.1 \pm 1.3	44.4 \pm 1.0
Avg. over Col	44.4 \pm 1.5	44.5 \pm 0.7	44.8 \pm 1.4	43.9 \pm 1.0	-

n_neighbors				
min_dist	5	15	50	100
0.05	-1.9	-2.8	-1.4	-0.9
0.1	-2.7	★	-0.1	-2.2
0.5	+0.4	-2.0	-1.5	-1.9
1.0	-1.5	-0.4	-0.8	-2.7

(a) Accuracy (over 5 runs)

(b) Accuracy Δ

D. Extended Empirical Results

D.1. Statistical Significance of Stability Improvements

To validate the stability benefits of TopoPrune (specifically, reduced variability in final model accuracy across independent runs), we conducted statistical tests focusing on high pruning rates (e.g., 90%), where coresnet selection variance is typically most pronounced. We compare TopoPrune against top-performing baselines, D2 (Maharana et al., 2024) and CCS (Zheng et al., 2023). Our analysis employed two complementary statistical approaches: (1) a one-tailed F-test to evaluate the hypothesis that TopoPrune exhibits lower variance than baselines ($\sigma_{\text{TopoPrune}}^2 < \sigma_{\text{baseline}}^2$), and (2) Bootstrapped 95% Confidence Intervals (CI) for the standard deviation of final accuracies, computed using 10,000 resamples with replacement.

As detailed in Table 8, on simpler datasets the difference in variance between methods is not statistically significant. However, for more challenging benchmarks, TopoPrune demonstrates statistically significant *p*-values ($p < 0.05$, bolded) for lower variance compared to both D2 and CCS. Also, the bootstrapped confidence intervals for the standard deviation

of TopoPrune are strictly lower, and in some cases disjoint, than those of the baselines. These findings confirm that our topological selection mechanism offers inherently superior stability compared to prior geometric methods.

Table 8. Statistical significance of variance at high pruning rate (90%) using **(a, b, c)** F-test shows TopoPrune’s lower variance is statistically significant for more difficult datasets. This is further validated by **(d)** TopoPrune’s tighter 95% confidence intervals of standard deviation.

p_value	CCS	D2	TopoPrune	p_value	CCS	D2	TopoPrune	p_value	CCS	D2	TopoPrune
CCS	0.500	~	~	CCS	0.500	~	~	CCS	0.500	~	~
D2	0.128	0.500	~	D2	0.437	0.500	~	D2	0.059	0.500	~
TopoPrune	0.422	0.094	0.500	TopoPrune	0.015	0.011	0.500	TopoPrune	0.012	0.001	0.500
(a) F-test on CIFAR-10				(b) F-test on CIFAR-100				(c) F-test on ImageNet-1K			
(d) Bootstrapped 95% confidence intervals of standard deviation											
95% CI	CIFAR-10	CIFAR-100	ImageNet-1K	95% CI	CIFAR-10	CIFAR-100	ImageNet-1K	95% CI	CIFAR-10	CIFAR-100	ImageNet-1K
CCS	[0.05, 0.91]	[0.85, 3.10]	[0.07, 0.75]	CCS	[0.05, 0.91]	[0.85, 3.10]	[0.07, 0.75]	CCS	[0.05, 0.91]	[0.85, 3.10]	[0.07, 0.75]
D2	[0.38, 1.77]	[0.26, 2.69]	[0.3, 2.12]	D2	[0.38, 1.77]	[0.26, 2.69]	[0.3, 2.12]	D2	[0.38, 1.77]	[0.26, 2.69]	[0.3, 2.12]
TopoPrune	[0.08, 0.35]	[0.1, 0.87]	[0.04, 0.23]	TopoPrune	[0.08, 0.35]	[0.1, 0.87]	[0.04, 0.23]	TopoPrune	[0.08, 0.35]	[0.1, 0.87]	[0.04, 0.23]

D.2. Roadmap of Detailed Experimental Results

Experiment / Ablation Topic	Main Section	Full Data Table
Overall Performance Across Baselines and Datasets	Section 4.2	Table 1
Transferability of <i>Diverse Embeddings</i> \rightarrow <i>Fixed Target</i>	Section 4.3	Table 10
Transferability of <i>Fixed Embedding</i> \rightarrow <i>Diverse Targets</i>	Section 4.3	Table 2
Stability to Noisy Feature Embeddings	Section 4.4	Table 9
Evaluation of Deep Topological Autoencoders	Section B.1.2	Table 3
Computational Complexity	Section B.3	Table 4, Table 5
Ablation: Differentiable Persistence Optimization Steps	Section C.1	Table 11
Ablation: Sensitivity of $(\alpha$ vs. β)	Section C.2	Table 12
Ablation: Training-Free Proxies for Mislabel Detection	Section C.3	Table 6
Ablation: Sensitivity to UMAP Hyperparameters	Section C.4	Table 7
Implementation Hyperparameters	~	Table 13

Table 9. Coreset performance under feature embedding noise on CIFAR-100. The plot shows mean accuracy vs. standard deviation (over 5 runs) for three geometric methods as noise (ϵ) and pruning rates increase. While Moderate is precise (low variance) but inaccurate and D2 is more accurate but imprecise (high variance), TopoPrune consistently delivers both high accuracy and high precision. The superiority of TopoPrune is most evident at the highest pruning rates and noise levels, highlighting its robustness. Best accuracy and standard deviation values are shown in bold. If more than one method have the same value, the second one is underlined.

Noise (\rightarrow)		$\epsilon \sim \mathcal{N}(0, 0.25\sigma)$				$\epsilon \sim \mathcal{N}(0, \sigma)$			
Pruning Rate (\rightarrow)		50%	70%	80%	90%	50%	70%	80%	90%
Moderate (Xia et al., 2023)	71.1 \pm 0.2	63.7 \pm 0.4	56.0 \pm 0.6	33.2 \pm 0.9	70.4 \pm 0.1	62.5 \pm 0.4	54.6 \pm 0.6	33.9 \pm 0.2	
D2 (Maharana et al., 2024)	72.8 \pm 0.1	68.5 \pm 0.7	63.0 \pm 0.5	44.4 \pm 1.5	73.0 \pm 0.1	67.7 \pm 1.2	62.3 \pm 0.8	40.2 \pm 2.0	
TopoPrune	73.5 \pm 0.3	67.8 \pm 0.1	60.5 \pm 0.2	45.4 \pm 0.8	73.3 \pm 0.2	68.0 \pm 0.5	62.7 \pm 0.3	45.5 \pm 0.6	
Noise (\rightarrow)		$\epsilon \sim \mathcal{N}(0, 4\sigma)$				$\epsilon \sim \mathcal{N}(0, 8\sigma)$			
Pruning Rate (\rightarrow)		50%	70%	80%	90%	50%	70%	80%	90%
Moderate (Xia et al., 2023)	71.0 \pm 0.4	62.9 \pm 0.3	52.3 \pm 0.6	32.0 \pm 1.2	70.9 \pm 0.2	63.4 \pm 0.2	51.6 \pm 2.2	32.1 \pm 1.4	
D2 (Maharana et al., 2024)	72.3 \pm 0.1	67.8 \pm 1.1	62.1 \pm 1.0	40.5 \pm 1.7	71.6 \pm 0.5	67.2 \pm 0.8	60.3 \pm 2.4	39.8 \pm 3.2	
TopoPrune	73.4 \pm 0.1	67.4 \pm 0.2	61.7 \pm 0.3	46.1 \pm 0.7	73.4 \pm 0.2	67.2 \pm 0.1	61.8 \pm 0.1	43.9 \pm 0.4	

Table 10. Transferability of Diverse Embeddings → Fixed Target. Features across many architectures to train a ResNet-18 model on CIFAR-100. Most models are taken from `torchvision` pretrained library which are finetuned from ImageNet-1K. We also look at the transferability of features from bigger OpenCLIP foundational models trained on the LAOIN-2b dataset (Schuhmann et al., 2022).

Pruning Rate (→)	50%			70%		
	Moderate	D2	TopoPrune	Moderate	D2	TopoPrune
ResNet-18 (He et al., 2016)	70.9±0.4	73.0±0.8	73.6±0.2	62.9±0.2	67.9±0.3	68.1±0.2
ResNet-50 (He et al., 2016)	71.1±0.1	73.0±0.2	73.7±0.2	63.3±0.4	67.7±0.4	68.0±0.1
ResNet-101 (He et al., 2016)	70.0±0.5	73.2±0.2	73.5±0.2	62.8±0.4	66.9±0.9	68.0±0.3
EfficientNet-B0 (Tan & Le, 2019)	71.6±0.3	73.2±0.2	72.9±0.2	62.9±0.1	67.5±0.4	67.5±0.2
EfficientNetV2-M (Tan & Le, 2021)	69.6±0.3	72.8±0.7	73.4±0.2	61.0±0.2	67.1±0.8	67.1±0.1
SwinV2-T (Liu et al., 2022)	70.5±0.1	73.6±0.1	73.6±0.2	60.4±0.6	66.9±1.0	67.6±0.1
SwinV2-B (Liu et al., 2022)	69.9±0.3	73.5±0.4	73.6±0.2	61.9±0.4	67.1±0.4	68.1±0.2
ViT-L-16 (Dosovitskiy et al., 2021)	69.8±0.3	73.3±0.3	73.6±0.1	61.5±0.3	67.2±0.6	68.0±0.1
OpenCLIP ViT-L-14 (Radford et al., 2021)	71.2±0.4	73.2±0.2	73.3±0.1	63.5±0.4	66.8±0.3	67.9±0.3
OpenCLIP ViT-H-12 (Radford et al., 2021)	70.9±0.3	73.0±0.2	73.1±0.4	62.4±0.3	66.6±1.3	67.7±0.2
(Schuhmann et al., 2022)						
Overall Average	70.6±0.3	73.2±0.3	73.4±0.2	62.3±0.3	67.2±0.7	67.8±0.2

Pruning Rate (→)	80%			90%		
	Moderate	D2	TopoPrune	Moderate	D2	TopoPrune
ResNet-18 (He et al., 2016)	54.8±0.2	60.3±1.9	60.2±0.2	33.8±0.8	42.5±1.9	43.4±0.4
ResNet-50 (He et al., 2016)	55.9±0.6	60.8±1.0	61.3±0.7	31.8±1.6	44.5±1.7	47.4±0.5
ResNet-101 (He et al., 2016)	54.5±0.4	60.4±0.2	60.0±0.6	35.9±0.6	41.7±2.6	43.2±1.3
EfficientNet-B0 (Tan & Le, 2019)	54.8±1.1	60.5±0.8	62.0±0.4	29.8±1.3	42.0±2.2	42.2±0.3
EfficientNetV2-M (Tan & Le, 2021)	53.1±0.5	60.2±0.4	60.1±1.6	33.3±0.8	41.3±1.9	44.4±1.7
SwinV2-T (Liu et al., 2022)	53.3±1.2	59.3±2.0	61.8±0.4	32.5±1.5	41.4±2.2	43.4±0.8
SwinV2-B (Liu et al., 2022)	53.5±0.2	60.2±1.5	61.1±0.6	35.7±0.3	42.8±2.9	42.7±1.6
ViT-L-16 (Dosovitskiy et al., 2021)	53.9±0.9	59.1±1.1	61.1±0.2	30.6±1.2	40.9±2.6	44.1±1.3
OpenCLIP ViT-L-14 (Radford et al., 2021)	53.9±0.8	60.4±1.0	61.7±0.8	35.0±1.5	40.7±2.9	42.5±1.6
OpenCLIP ViT-H-12 (Radford et al., 2021)	54.0±0.8	61.1±0.4	61.8±0.8	35.4±1.4	42.3±2.1	42.9±1.0
(Schuhmann et al., 2022)						
Overall Average	54.2±0.7	60.2±1.0	61.1±0.6	33.4±1.1	42.0±2.2	43.6±1.1

Table 11. Persistent Homology optimization steps on CIFAR-10. Optimal in bold, ties are underlined.

# Steps	Pruning Rate (%)				
	30%	50%	70%	80%	90%
1	94.8±0.1	93.5±0.2	90.8±0.2	86.2±0.4	77.1±0.6
2	<u>94.9±0.1</u>	93.8±0.3	90.9±0.5	86.7±0.1	79.6±0.5
4	94.5±0.2	93.7±0.2	90.9±0.1	87.5±0.5	80.8±0.5
6	94.9±0.1	93.7±0.1	91.2±0.1	89.0±0.3	81.5±0.3
11	94.6±0.1	93.6±0.1	91.6±0.2	88.6±0.3	80.5±0.5
21	94.8±0.1	93.5±0.2	91.3±0.2	88.7±0.2	80.7±0.8
31	94.7±0.2	93.7±0.1	91.4±0.2	88.3±0.1	80.7±0.6
41	<u>94.9±0.1</u>	93.6±0.2	<u>91.6±0.2</u>	88.8±0.5	80.4±0.7
51	94.7±0.2	93.7±0.2	91.4±0.1	88.1±0.7	81.8±0.3

Table 12. Hyperparameters for local persistence (α) and global density (β). While our fixed 50/50 split provides strong, stable performance, the results indicate that further accuracy gains are possible with task-specific tuning. We observe a trend where the optimal balance increasingly relies on the persistence score (α) on more challenging datasets (e.g., CIFAR-100 vs. CIFAR-10) and at higher data pruning rates. Optimal results are in bold, ties are underlined.

CIFAR-10		Pruning Ratio (%)					CIFAR-100		Pruning Ratio (%)				
α/β		30%	50%	70%	80%	90%	α/β		30%	50%	70%	80%	90%
100/0		94.7 \pm 0.1	93.2 \pm 0.1	90.6 \pm 0.1	87.9 \pm 0.4	80.4 \pm 0.1	100/0		75.7 \pm 0.2	73.2 \pm 0.2	67.4 \pm 0.2	59.8 \pm 0.9	43.2 \pm 0.3
90/10		94.3 \pm 0.1	93.1 \pm 0.1	90.4 \pm 0.3	88.3 \pm 0.1	79.9 \pm 1.2	90/10		76.4 \pm 0.3	73.0 \pm 0.1	66.8 \pm 0.7	60.8 \pm 0.5	43.0 \pm 0.5
80/20		94.7 \pm 0.1	93.3 \pm 0.1	90.8 \pm 0.2	89.0 \pm 0.2	79.3 \pm 0.9	80/20		76.5 \pm 0.1	73.1 \pm 0.4	67.5 \pm 0.1	61.8 \pm 0.2	47.2\pm1.6
70/30		94.4 \pm 0.2	93.6 \pm 0.1	90.7 \pm 0.2	88.5 \pm 0.1	78.9 \pm 1.2	70/30		76.0 \pm 0.2	72.9 \pm 0.6	67.7 \pm 0.2	61.5 \pm 0.3	45.2 \pm 0.7
60/40		94.5 \pm 0.3	93.5 \pm 0.3	91.3 \pm 0.1	87.8 \pm 0.2	81.3 \pm 0.6	60/40		76.0 \pm 0.2	73.3 \pm 0.3	67.1 \pm 0.7	60.6 \pm 0.8	44.8 \pm 1.2
50/50		94.7 \pm 0.2	93.7 \pm 0.2	91.6\pm0.1	88.7 \pm 0.7	82.1 \pm 0.3	50/50		75.9 \pm 0.4	72.8 \pm 0.3	66.9 \pm 0.5	61.9 \pm 0.6	45.8 \pm 0.7
40/60		94.6 \pm 0.3	93.3 \pm 0.1	91.4 \pm 0.2	88.6 \pm 0.2	80.3 \pm 0.5	40/60		76.5 \pm 0.1	73.7 \pm 0.3	67.9 \pm 0.1	62.5\pm0.3	43.1 \pm 0.6
30/70		94.9 \pm 0.1	93.9\pm0.3	91.4 \pm 0.2	89.0 \pm 0.3	82.0 \pm 0.1	30/70		76.6 \pm 0.1	74.0\pm0.2	67.9 \pm 0.7	62.4 \pm 0.6	43.4 \pm 0.5
20/80		95.0\pm0.1	93.8 \pm 0.1	91.3 \pm 0.2	88.9 \pm 0.1	82.3 \pm 0.5	20/80		77.1\pm0.1	<u>74.0\pm0.2</u>	68.1\pm0.1	62.2 \pm 0.3	45.4 \pm 2.8
10/90		94.8 \pm 0.1	93.7 \pm 0.2	91.0 \pm 0.5	89.3\pm0.2	82.7\pm0.1	10/90		76.7 \pm 0.2	73.6 \pm 0.3	67.3 \pm 0.3	61.4 \pm 0.7	40.9 \pm 1.9
0/100		94.9 \pm 0.1	93.8 \pm 0.1	91.3 \pm 0.1	89.1 \pm 0.2	82.2 \pm 0.4	0/100		76.2 \pm 0.1	73.5 \pm 0.2	67.8 \pm 0.2	61.5 \pm 0.7	41.8 \pm 0.6

Table 13. (a) Training and topological hyperparameters. **(b)** Dataset mislabel ratios.

Section	Hyperparameter	CIFAR-10		ImageNet		Pruning	Mislabel Ratio (%)		
		CIFAR-100	CIFAR-100	Cosine	Annealing		C-10	C-100	ImageNet
Training (DeepCore)	Epochs	200		60		30%	0%	10%	0%
	Batch Size	256		128			0%	20%	10%
	Optimizer	SGD		SGD			10%	20%	20%
	Momentum	0.9		0.9			10%	40%	20%
	Learning Rate	1e-1		1e-1			30%	50%	30%
	Weight Decay	5e-4		5e-4					
Global Manifold Projection (UMAP)	Scheduler	Cosine	Annealing	Cosine	Annealing	50%	0%	20%	10%
	Number Neighbors	15		15			0%	20%	10%
	Minimum Distance	0.1		0.1			10%	20%	20%
	Metric	Cosine		Cosine			10%	40%	20%
Kernel Density Estimation (sklearn)	Dimensions	2		2		70%	10%	20%	20%
	Bandwidth	0.4		0.4			10%	20%	20%
	Theta (Density Bandwidth)	0.4		0.4			30%	50%	30%
Local Persistent Homology (multipers)	Function/Kernel	Gaussian		Gaussian		80%	0%	20%	10%
	Complex	Weak-Delaunay		Weak-Delaunay			0%	20%	10%
	Homology Degree	1		1			10%	20%	20%
	Optimization Steps	6		6			10%	40%	20%
Topology Score	Global Density (α)	0.5		0.5		90%	30%	50%	30%
	Local Persistence (β)	0.5		0.5					
NLPS (KNN sklearn)	Number Neighbors	20		20					

(a) Training and topological hyperparameters. (b) Dataset mislabel ratios. Similar to those in [Zheng et al. \(2023\)](#).